Bonner Zentrum für Lehrerbildung (BZL)

Evolution of Massive Contact Binaries

Bachelorarbeit im Fach Physik
für das Lehramt an Gymnasien und Gesamtschulen

vorgelegt von
Kai Uwe Förster

Matrikelnummer: 3082262

betreut durch
Prof. Dr. Norbert Langer

Zweitgutachter:
Prof. Dr. Frank Bertoldi

angefertigt im
Argelander-Institut für Astronomie
der Rheinischen Friedrich-Wilhelms-Universität Bonn

Sommersemester 2023
Bonn, den 06.11.2023

Ich versichere hiermit, dass die Bachelorarbeit mit dem Titel „Evolution of Massive Contact Binaries“ von mir selbst und ohne jede unerlaubte Hilfe selbständig angefertigt wurde, dass sie noch an keiner anderen Hochschule zur Prüfung vorgelegen hat und dass sie weder ganz noch in Auszügen veröffentlicht worden ist. Die Stellen der Arbeit – einschließlich Tabellen, Karten, Abbildungen usw. –, die anderen Werken dem Wortlaut oder dem Sinn nach entnommen sind, habe ich in jedem einzelnen Fall kenntlich gemacht.

Bonn, ...

Datum Unterschrift

1. Gutachter: Prof. Dr. Norbert Langer
2. Gutachter: Prof. Dr. Frank Bertoldi

Abstract

Most close massive binary stars with initial periods of a few days go through a contact phase, during which both stars simultaneously overflow their Roche lobes. Previous work exhibits a discrepancy between stellar evolution models and observational constraints, in mass ratio among others, indicating that some physics must be missing from the models. This work aims to alleviate this discrepancy by investigating in the effect of rejuvenation on the overall mass ratio evolution. A set of 12 new detailed binary evolution models is computed, by taking an evolution model from previous work as a starting point, and varying the levels of rejuvenation efficiency. The results show that rejuvenation has a considerable impact on the overall mass ratio evolution, and can affect the longevity of the models at a mass ratio close to 1. The way in which the mass ratio evolution is affected varies depending on the type of mixing process that causes the rejuvenation.

Acknowledgements

Especially, I would like to thank Prof. Dr. Norbert Langer for his initial idea for this thesis and for his continuous patience with sharing his knowledge, turning the work progress into an absorbing process of exploration.

Also, Dr. Athira Menon stood by my side in this journey, next to providing the paper, giving me incredibly valuable advice. I would also like to thank everybody from the stellar research group in the Argelander Institute who supported this work at various occasions.

Ultimately, my gratitude goes above all to my parents, my family, my friends and teachers, who inspired me and got me through all the difficult phases, especially during my studies, and who ultimately made me the person I am.

Contents

CHAPTER 1

Introduction

When observing the star-spattered sky with the unaided eye, numerous light sources appear as single stars. Using different tools (e.g. spectra or light curves) many of these light sources turn out to be two separate star components orbiting around each other. Even more, some of them can be – using a top-quality telescope – visually resolved as two separate components. These gravitationally bound star systems are called *binary stars*. In fact, it turns out that over half of the stars are found in binary or even multiple star systems. Investigating in binary evolution is an essential part of stellar astrophysics in order to understand black holes and pulsars with stellar companions, binary progenitors of gravitational waves and X-ray binaries among others. Moreover, binary stars may also provide strong constraints on internal stellar mixing processes, which still need to be calibrated properly (Pols, 2009).

The evolution of binary stars is predominantly dependent on the Roche lobe overflow of the two components. The Roche lobe of a star is a three-dimensional equipotential surface through the inner Lagrangian point L_1, where all forces cancel out (cf. fig. 3.1). Material within the Roche lobe is gravitationally bound to the star. Stars typically expand during hydrogen burning. If the initial orbital separation of two binary components is big enough, the Roche lobe is large enough to ensure that the stellar radius never overflows. Hence, they evolve as if they were single stars. In contrast, close binaries with periods of only a few days (and small orbital separations) may overflow their respective Roche lobes (Eggleton, 1983). Typically, mass is transferred from the star that overflows its Roche lobe (called the "donor"), via the Lagrangian point L_1 to its companion (called the "accretor"). When both stars simultaneously overflow their Roche lobes, they "touch" each other, forming what is known as a contact binary with a shared common surface, as depicted in fig. 1.1. At contact, mass is transferred to the amount, so that both stellar components overflow their Roche lobes to the same degree. This thesis focuses on the evolution of massive contact binaries burning hydrogen in their cores. Both stars have masses $> 10\,\mathrm{M}_\odot$ and they may share a common surface over a nuclear timescale for millions of years. Such contact binaries have been observed in our satellite galaxies – the Large (LMC) and the Small Magellanic Clouds (SMC) – as well as in our Milky Way. A significant fraction of massive binary stars may end up merging to form new stars (de Mink et al., 2013). These can lead to exciting phenomena like peculiar supernovae, which single-star models find challenging to explain (Marchant et al., 2016).

Menon et al., 2021 performed the first detailed study of massive contact binaries, by computing 5580 binary evolution models with the stellar evolution code MESA (Modules for Experiments in Stellar Astrophysics, Paxton, Bildsten et al., 2011 - Jermyn et al., 2023) over a range of initial binary parameters, for the LMC and SMC. They found that stellar evolution models remaining in contact for a long time undergo mass exchange – so that their components evolve towards having equal masses. As a consequence, these models spend a considerable amount of time at mass ratios close to one (i.e.

Figure 1.1: An artist's impression of the massive contact binary VFTS 352 in the Large Magellanic Cloud. Credits: *ESO/L. Calçada* 2023

both components almost have the same masses). If these models reflected reality, most of the observed contact systems should also be found at a mass ratio close to one. Spectroscopic surveys of eclipsing binaries have found 2 massive contact binaries in the SMC, around 40 in the LMC and 17 in the Milky Way so far. The reported mass ratios q for most of these systems were < 0.9, which was in contradiction with the findings of Menon et al., 2021. This discrepancy could be alleviated when accounting for the possibility that the reported contact binaries are not exactly in contact but only nearing contact, in which case the mass ratios of most of the observed systems are explained properly (Menon et al., 2021). But still, there are less massive contact binaries observed at a mass ratio close to one than expected from the findings of Menon et al., 2021. Consequently, some physics must be missing from their contact binary evolution models in order to be able to reflect reality.

There have already been first approaches to understand this discrepancy by Fabry et al., 2023: They expect heat transfer to happen from one stellar component to another, as two stars with different total masses have different surface temperatures. Because the two stars "touch" each other, the different temperatures may equalize.[1] When heat is transferred, the radius of the stellar component is affected. That again influences the amount of mass that is transferred from one component to another and therefore affects the evolution of mass ratio. Fabry et al., 2023 incorporated heat transfer during contact phases so that temperature is constant along a stellar layer within the common envelope. With the computation of one contact binary model, they found that the mass ratio can diverge from 1, for a longer timescale than the models of Menon et al., 2021.

This thesis investigates an alternative physics process which considers the rejuvenation of the hydrogen burning core, which may affect the mass ratio evolution. In a single main sequence star (i.e. it burns

[1] In Menon et al., 2021 heat transfer was not included, arguing that surface temperatures of the stellar components typically differ by less than 20%.

hydrogen), the central hydrogen abundance decreases with time and the core contracts in mass. When a star in a binary system (during main sequence) gains mass from its companion, it triggers convection instabilities which can expand the core and mix in some of the material just above the core, which has a higher hydrogen abundance than the core itself. Depending on the efficiency of the mixing, the mass gain may lead either to a rejuvenation and an expansion of the core, or even to a prevention of it, causing the core not to respond to the accretion and continuing its contraction (Braun and Langer, 1995).

The efficiency of rejuvenation and its effects on binary evolution is not well constrained, particularly in the case of contact binaries. An effective rejuvenation during mass transfer in a contact configuration is expected to be associated with the evolution towards having equal masses: If both stars reach a mass ratio of 1 (i.e. they have the same total masses) and are rejuvenated effectively to the same degree, their radii will also be equal. They overflow their Roche lobe to the same degree and no mass is transferred. The mass ratio remains at one. This situation may change depending on the efficiency of rejuvenation, which may lead to stars with equal masses to have different radii and thereby cause a mass transfer from the more expanded star to its companion. In short, an evolution towards a mass ratio close to one is expected if rejuvenation occurs effectively throughout the evolution. It is expected to be prevented if rejuvenation does not occur.

The aim of this thesis is to investigate in the effect of rejuvenation to the overall mass ratio evolution of contact binaries. First, the efficiency of rejuvenation is considered in a contact binary model of Menon et al., 2021, and how it could affect the longevity of the models at a mass ratio close to 1. A set of new models is computed, corresponding to the "System 2" exemplary model in their paper, by only varying the levels of rejuvenation efficiency. It is explored how they evolve until the end of the main sequence or until they merge.

This thesis is divided into the following chapters: Chapter 2 gives a short introduction to the most relevant basics in theory. Chapter 3 shows the relevant methods and physical assumptions that are implemented in the stellar evolution code in order to compute the binary evolution models, as well as the tools that are used to evaluate the results. Chapter 4 deals with the results. They are discussed in chapter 5 and summarized in chapter 6.

This work will open up a new direction for prospective studies that may be intended to calibrate the exact mixing physics by calculating large grids of binary evolution models. Moreover, it may help solve the discrepancy between the predictions of current models and the properties of observed contact binaries.

CHAPTER 2

Mixing and Mass Transfer in Massive Stars

This chapter is intended to give a short introduction to the most relevant basics in theory. Sections 2.1 until 2.3 feature the mixing processes that are used in this thesis in order to modify the efficiency of rejuvenation. Sections 2.4 and 2.5 deal with basic concepts of binary interaction.

2.1 Convection

The following paragraphs are based on Pols, 2009.

Thermal motions of gas particles naturally cause small fluctuations from spherical symmetry. Considering an upwards displaced mass element, its density will decide about these initial fluctuations to grow or to stay negligible: If the upwards displaced mass element is denser than its surrounding, it will fall back into the direction of its original position. In this case, the layer is said to be *dynamically stable*. If it is less dense than its surrounding, the buoyancy force will lead to a growing upwards displacement. An initially small fluctuation is then enough to displace a gas element over a macroscopic distance. The layer is said to be *dynamically unstable*.

Hence, convection can be described as "cyclic macroscopic motions of [gas bubbles]" (Pols, 2009) due to dynamical instability. The gas bubbles move up (down), until they dissolve and emit (absorb) their heat to the surrounding, analogously with their chemical composition. Therefore, convection is an efficient process of heat transport and mixing. The radial distance, over which the gas bubbles travel, until they resolve into their surroundings, is commonly called the "mixing length" l_{m}. The exact value for l_{m} is unknown. But it is assumed to be in the order of the local pressure scale height H_{p}, where H_{p} is the distance, over which the pressure undergoes a change by a factor of e.

The previously elucidated condition for dynamical stability (the density of the displaced gas element is bigger than the density of its surrounding) can be mathematically rephrased to the *Ledoux criterion for stability against convection*: A stellar layer is stable against convection, if

$$\nabla_{\mathrm{rad}} < \nabla_{\mathrm{ad}} + \nabla_{\mu} \tag{2.1}$$

holds (for an ideal gas), where ∇_{rad} (the radiative temperature gradient) is a spatial temperature gradient that a star in a hydrostatic equilibrium has, if energy was transported only by radiation. The non-spatial adiabatic temperature gradient ∇_{ad} describes the behavior of temperature under adiabatic compression

or expansion of a gas element. The other relevant gradients can be defined as

$$\nabla := \left(\frac{\mathrm{d}\ln T}{\mathrm{d}\ln P}\right)_{\mathrm{s}}, \quad \nabla_{\mathrm{e}} := \left(\frac{\mathrm{d}\ln T}{\mathrm{d}\ln P}\right)_{\mathrm{e}}, \quad \nabla_{\mu} := \left(\frac{\mathrm{d}\ln \mu}{\mathrm{d}\ln P}\right)_{\mathrm{s}}. \tag{2.2}$$

∇ is the actual spatial temperature gradient of the surrounding. $\nabla = \nabla_{\mathrm{rad}}$ consequently holds for a radiative envelope. ∇_{e} is the actual non-spatial temperature gradient of the gas element. It describes the behavior of the temperature of the gas element under compression or expansion. $\nabla_{\mathrm{e}} = \nabla_{\mathrm{ad}}$ holds for adiabatic behavior of the gas element. ∇_{μ} is the spatial gradient of mean molecular weight throughout the star.

Coinciding with the models in this thesis, massive stars are expected to have convective cores, as

$$\nabla_{\mathrm{rad}} \propto \kappa \frac{l}{m}, \tag{2.3}$$

where l is the local luminosity, m is the mass coordinate and κ the opacity. Nuclear energy generation in massive stars is strongly peaked towards the center (i.e. they have a big l/m in the stellar center), because the temperature sensitive CNO-cycle dominates the nuclear energy generation. That leads to a rapid drop of nuclear energy generation, when temperature decreases outwards the center. Consequently, ∇_{rad} drops going further away from the center. Dynamical instability is halted at the threshold $\nabla_{\mathrm{rad}} = \nabla_{\mathrm{ad}} + \nabla_{\mu}$. The extent of the convective core is essential, as it defines the amount of burning material that is available. Convection effectively mixes unprocessed material to the zones of nuclear energy generation.

The convective core retracts during burning hydrogen: The amount of helium in the core grows and the mean molecular weight μ rises. As $\kappa \propto \mu^{-1}$, the opacity decreases. That leads to a decrease of ∇_{rad} (cf. eq. 2.3) and a retraction of the threshold, where $\nabla_{\mathrm{rad}} = \nabla_{\mathrm{ad}} + \nabla_{\mu}$. The amount of hydrogen decreases during nuclear burning. Consequently, the retracting core leaves behind a composition gradient reflecting the evolution of its chemical composition.

2.2 Overshooting

This section features the main aspects of the mixing process called “overshooting”. It is based on Pols, 2009 unless otherwise indicated.

As described in section 2.1, the buoyancy force on a displaced element vanishes at the boundary of the convective zone, where

$$\nabla_{\mathrm{rad}} = \nabla_{\mathrm{ad}} + \nabla_{\mu}. \tag{2.4}$$

Inside this boundary (within the convective core) the buoyancy force on a gas element exerts upwards, outside this boundary it exerts downwards[1]. As soon as an upwards moving gas bubble reaches the boundary, it will not immediately stop due to its inertia. Instead, it *overshoots* the boundary and its motion gets constantly slowed down due to the now inside directed buoyancy force. The distance, over which the overshooting gas bubbles penetrate into the envelope (from now on called the “extent of the overshooting region”), is not certainly known from theory. Analogously to the mixing length in section 2.1, it is commonly parametrized by a fraction of the local pressure scale height H_{p} at the boundary of

[1] Downwards means in the direction to the stellar center, upwards means the direction to the stellar surface.

the convective core.

Although the extent of the overshooting region is poorly determined, it has a considerable impact on stellar evolution: A larger overshooting region mixes more burning material into the convective core, with the consequence that hydrogen burning lasts longer. In addition to that, it increases the luminosity as well as the radius of the star, leading to a considerable impact on the fate of binary stars (cf. section 2.5).

As described in the previous section 2.1, the retracting convective core of massive stars leaves behind a gradient in mean molecular weight. That does not change when accounting for overshooting, as the overshooting region is expected to recede analogously. When a star gains mass from its companion, the boundary, where eq. 2.4 holds, will move outwards in mass, causing the overshooting region to encounter the previously left behind composition gradient. When considering an overshooting gas bubble penetrating into a region of such a composition gradient, the gas bubble consists of quite processed material from the core. On the contrary, the composition gradient of the surrounding leads to a continuous decrease in mean molecular weight in the outward direction. Consequently, the density of the gas bubble is considerably higher than the density of its surrounding. That continuously increases the downward buoyancy force. Hence, a composition gradient operates as a stabilizing effect against overshooting (Marchant, 2018, sec. 5.1.2).

2.3 Semiconvection

Semiconvection is the third mixing process that is relevant for this thesis. The following paragraphs are based on Kippenhahn, Weigert and Weiss, 2012.

In a dynamically stable layer (i.e. a radiative envelope, cf. section 2.1), an upwards displaced element will fall back into the direction of its original position. Arrived at the original position, it has a momentum causing the element to exceed its original position. Under the assumption of adiabatic compression and expansion, as well as neglecting drag forces (due to the small deflection) the mass element starts to oscillate around its original position with a constant amplitude, coinciding with its original displacement.

Considering a deviation from adiabatic expansion has an effect on the amplitude of the oscillating gas element. The following case differentiation consequently takes ∇ instead of ∇_{rad}, and ∇_{e} instead of ∇_{rad}, as defined in eq. 2.2.

- $\nabla < \nabla_{\mathrm{e}}$
  In this case, the upwards displaced element has a smaller density, coinciding with a smaller temperature than its surrounding. The element receives energy by radiation from its surrounding, and the difference in density gets smaller (as it gains temperature). That leads to a smaller downward buoyancy force (analogously with the downward displacement). An oscillation with a slowly decreasing amplitude is the consequence. In this case, one speaks of *vibrational stability via radiative damping*.

- $\nabla_{\mathrm{e}} < \nabla < \nabla_{\mathrm{e}} + \nabla_{\mu}$
  Without the stabilizing composition gradient ∇_{μ}, the upwards displaced element would have a smaller density and a higher temperature than its surrounding, causing it to be dynamically

unstable. Because of the composition gradient, the density of the mass element is still higher than its surrounding, so that the element remains dynamically stable. But the composition gradient does not change the difference in temperature! In contrast to the first case, the upwards displaced element loses energy by radiation to its surrounding. The mass element gets cooler, its density increases, and the downward buoyancy force grows. That causes a gaining of additional momentum. The amplitude of the oscillation around its original position rises. In this case, one speaks of *vibrational instability* or *over-stability* via *radiative amplification*.

Semiconvection is considered as a slow mixing process due to vibrational instability. Although there are approaches to parametrize the growth rate of the amplitude of the oscillating gas element (cf. sec. 3.1), it is not reliably known from theory, so that the efficiency of semiconvection is a free parameter in stellar evolution codes. Due to its nature as vibrational instability, semiconvection only occurs in the presence of a composition gradient. In particular for the models in this thesis: Within the regions of the composition gradient that the contracting convective core leaves behind (as described in sec. 2.1). Since the oscillating gas elements lead to a chemical mixing when they dissolve, the composition gradient can be smoothed via semiconvective mixing, depending on its efficiency, possibly causing dynamical instabilities, so that new convection zones emerge.

2.4 Classification of Close Binary Systems

This section gives an overview of several basic terms and the different classifications of a binary. It is based on Boer, 2008.

A binary star system contains two components, called the *primary* (with the mass M_1) and the *secondary* (with the mass M_2, where the primary (secondary) is the initially more (less) massive star. Whenever a component releases mass to its component, it is called the *donor*. When a component gains mass from its companion, it is called the *accretor*.

The gravitational potential from a binary can be extracted from fig. 2.1. Especially considering the Roche lobe, the three-dimensional equipotential surface going through the inner Lagrangian point L_1, is most important for the overall fate of a contact binary. Depending on the rate of Roche lobe overflow, three distinct configurations are distinguished (cf. fig. 2.2): Systems where both stellar components remain within their Roche lobes are called a *detached* systems. When only one component overflows its Roche lobe, they are in a *semi-detached* configuration. When both stars fill their Roche lobes, they are called *contact binaries*. An *over-contact* configuration is usually understood as both stars overflowing their Roche lobes simultaneously. In this thesis, contact and over-contact configurations are handled synonymously.

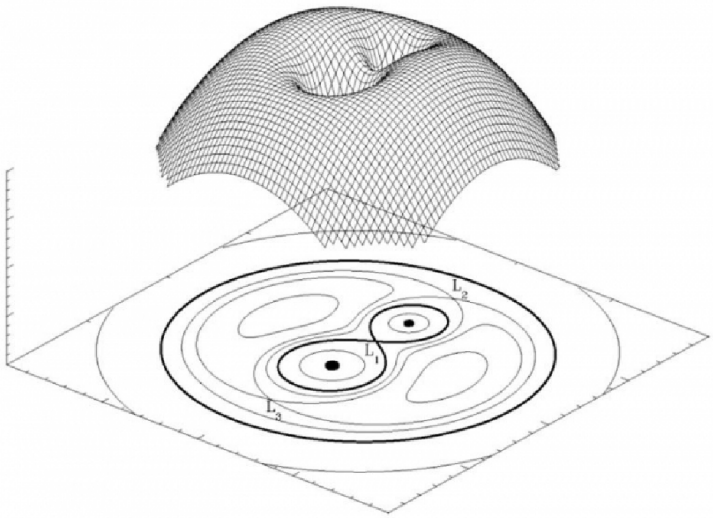

Figure 2.1: Equatorial cross section of equipotential surfaces in a binary with mass ratio $q = 0.5$, together with a three-dimensional representation of the potential. Equipotential lines going through the inner Lagrangian point L_1 indicate the 2-D representation of the Roche lobe. Credits: Postnov and Yungelson, 2014.

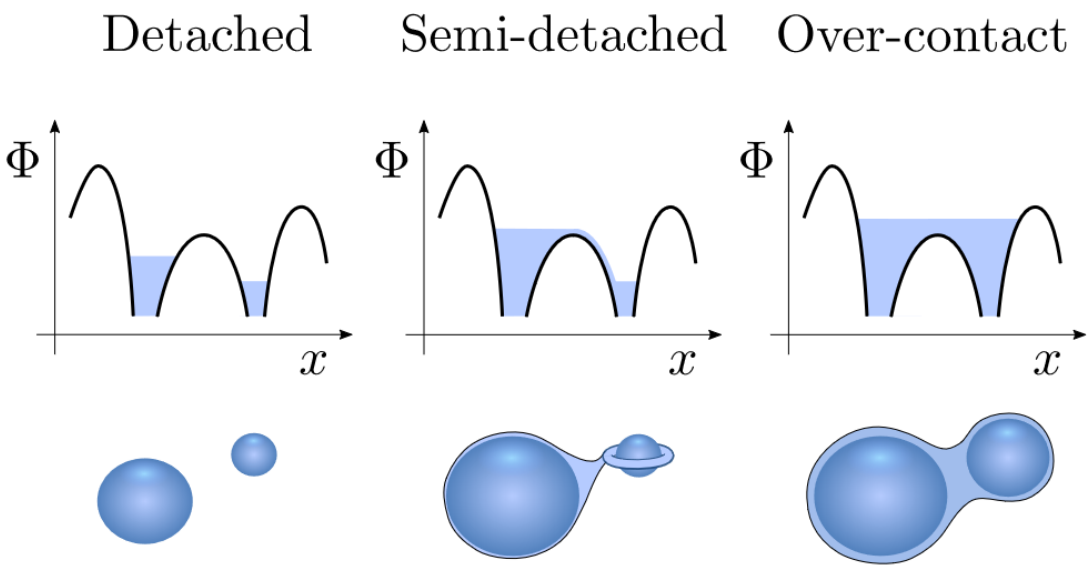

Figure 2.2: Possible binary configurations in terms of Roche lobe overflows. Φ is the gravitational potential along the line joining both components, parametrized by x. Credits: Marchant, 2018

2.5 Binary Mass Transfer

This section is based on Postnov and Yungelson, 2014, if not stated differently.

During the main sequence, the mean molecular weight μ increases due to hydrogen burning. Because the radius

$$R \propto \mu^{0.67} M^{0.81} \tag{2.5}$$

(for hydrogen burning dominated by the CNO cycle (Pols, 2009)) is proportional to μ, stellar radii do increase during main sequence. The radius of the Roche lobe (corresponding to eq. 3.1) of a binary component with mass M_1 can be estimated to

$$\frac{R_{\mathrm{L1}}}{a} = 0.38 + 0.2 \log\left(\frac{M_1}{M_2}\right), \tag{2.6}$$

where a is the orbital separation between the components (Boer, 2008). Consequently, binaries with smaller orbital separations have smaller respective Roche lobe radii, so that mass transfer via Roche lobe overflow may happen.

When only one component overflows its Roche lobe, mass is transferred to that rate that the donor remains inside its Roche lobe. When both stars are in contact, mass is transferred to that amount so that both stars overflow their Roche lobe to the same degree.

Mass transfer from the less massive to the more massive star is fundamentally different: The initially more massive star in a binary evolves faster than the secondary. Typically, it will fill its Roche lobe first. When the more massive star transfers mass to the less massive star, the orbital separation will decrease due to considerations of conservation of angular momentum. That also decreases the Roche lobe radius (cf. eq. 2.6), causing even more mass to be transferred. That potentially leads to an instable case, where mass is transferred on a thermal timescale[2]. When the less massive star transfers mass to the more massive star, the orbital separation will rise, leading to an increase in the Roche lobe radius. There is no “feedback loop” in mass transfer, and the mass transfer rate is only up to the nuclear expansion of the donor, so that mass is transferred on a nuclear timescale. This type of mass transfer leads to a semi-detached configuration.

[2] The radius of the donor reacts to mass loss on a thermal timescale

CHAPTER 3

Methods

In this thesis, the stellar evolution code MESA (Modules for Experiments in Stellar Astrophysics) is employed – specifically, version 10398. Although it is not the most recent one, this version is chosen to ensure comparability with the results presented in Menon et al., 2021[1]. MESA simulates stellar evolution models in one dimension, basically by solving differential equations of stellar structure as described in the MESA instruments papers (Paxton, Bildsten et al., 2011; Paxton, 2013; Paxton, Marchant et al., 2015; Paxton, Schwab et al., 2018; Paxton, Smolec et al., 2019; Jermyn et al., 2023).

As the parameter setup in the starting point model is adopted (see section 3.3), stellar physics in the models for this thesis are exactly the same as described in section 2.1 of Menon et al., 2021. The models only differ in the two mixing processes overshooting and semiconvection. Sections 3.1 & 3.2 are intended to summarize the main features of the physical assumptions made in Menon et al., 2021 that are relevant for this thesis. Section 3.3 will declare the initialization of the models for this thesis. The rest of this chapter (sections 3.4 - 3.6) gives an account of the tools that are used to evaluate the results.

3.1 Mixing

Overshooting and semiconvection are affected by three different mixing parameters (α_{ov}, α_{sc} and B). The way MESA uses these parameters, and therefore how it treats the two mixing processes, is summarized below.

In terms of mixing processes, a hydrodynamical simulation in 3 dimensions is possible but computation-intensive. Instead, MESA implements mixing types like convection, overshooting and semiconvection as one-dimensional diffusive processes (for example, cf. section 5.2 in Paxton, Bildsten et al., 2011). The efficiency of the different mixing processes is consequently described by their diffusion coefficients according to Fick's laws of diffusion (Kippenhahn, Weigert and Weiss, 2012).

Semiconvection is included as described in Langer, Fricke and Sugimoto, 1983. α_{sc} – the semiconvection efficiency parameter – affects the growth rate of the amplitudes of an oscillating gas element in a vibrational instable layer (see sec. 2.3). The semiconvective diffusion coefficient is proportional to α_{sc}. Thereby α_{sc} can be handled as a dimension of efficiency for semiconvection.

Overshooting is treated using a step overshoot scheme: The overshooting region extends the distance $\alpha_{\mathrm{ov}} * H_{\mathrm{P}}$ from the location r_0 where $\nabla_{\mathrm{rad}} = \nabla_{\mathrm{L}}$ into the envelope, where H_{P} is the local pressure scale

[1] The necessary files to reproduce the models calculated in this thesis are provided at `https://github.com/WhiteDwarf98/evolution_of_massive_contact_binaries.git`.

height and ∇_{ad}, ∇_{rad} are the adiabatic and radiative temperature gradients, respectively. α_{ov} is called the step overshooting parameter. In contrast to α_{sc}, it is only about the extent of the overshooting region, but not about the efficiency within the region. Instead, the efficiency is again defined by the overshoot mixing diffusion coefficient. This diffusion coefficient is taken from the edge of the convective zone and extended beyond the zone, assuming it to be constant. That means the efficiency of mixing through step overshooting at the top and the bottom of the overshooting region is the same - in contrast to an exponential overshooting scheme, where mixing at the top is less effective than at the bottom close to the convection zone (*MESA documentation* 2023).

B – commonly called the Ledoux term (e.g. Paxton, 2013) – is another parameter that is used in order to affect overshooting. It serves as a threshold for the composition gradient, beyond which overshooting is halted (*MESA documentation* 2023). This is considered to be legitimate, because a composition gradient increases the restoring force that a gas element experiences when it overshoots the convective core (as described in sec. 2.2). Therefore, a composition gradient can constrain the extent of the overshooting region. B is used besides α_{ov}, because the step overshooting scheme is insensitive to the stabilizing effect of a composition gradient (Marchant, 2018, section 5.1.2). Overshooting can erase the composition gradient in places where semiconvection would otherwise have occurred (as shown in section 4.1). This thesis is also intended to investigate in the effect of semiconvection, hence the composition gradient cannot be ignored. In other contexts the term B is also directly called like the local composition gradient ∇_μ (for example in Boer, 2008) or even f (in Marchant, 2018). In this thesis, it is called B, having its letter from his contribution to the **B**runt–Väisälä frequency (following Paxton, 2013).

3.2 Contact Phase

The following summarizes the key attributes of the implementation of contact phases in MESA, following the approach detailed in Marchant, 2018 and Marchant et al., 2016.

In a contact binary, stellar matter is not spatially separated. Hence, for allocating a volume to each component, it is divided in two separate volumes by a plane through the inner Lagrange point L_1 as shown in fig. 3.1. Each volume ($V_1(\Phi), V_2(\Phi)$) is associated with a volume equivalent radius ($R_1(\Phi), R_2(\Phi)$) – the radius the star would have, if it were a uniform sphere with the same mass that the actual star has, within the equipotential surface Φ. The Roche lobe radius

$$R_{RL} = R(\Phi(L_1)) \tag{3.1}$$

is consequently defined as the volume equivalent radius at the potential at L_1.

Spherical symmetry is a good approximation for most single stars isolated in space, as it arises from self-gravity (Pols, 2009). Calculating the stellar evolution in one dimension is consequently assumed to provide stellar properties (e.g. temperature, density, composition) for the star as a whole as they only depend on the radius under the assumption of spherical symmetry. At the latest, when considering binary stars in contact, the assumption of spherical symmetry cannot hold. Instead, the photospheres of the binary components lie on a three-dimensional equipotential surface, as depicted in fig. 3.1. Every component (on its own) assumed to be shellular (following the definition of Fabry et al., 2023): "[A]ll intensive quantities, in particular the temperature, pressure and mass density, are constant along [...] a

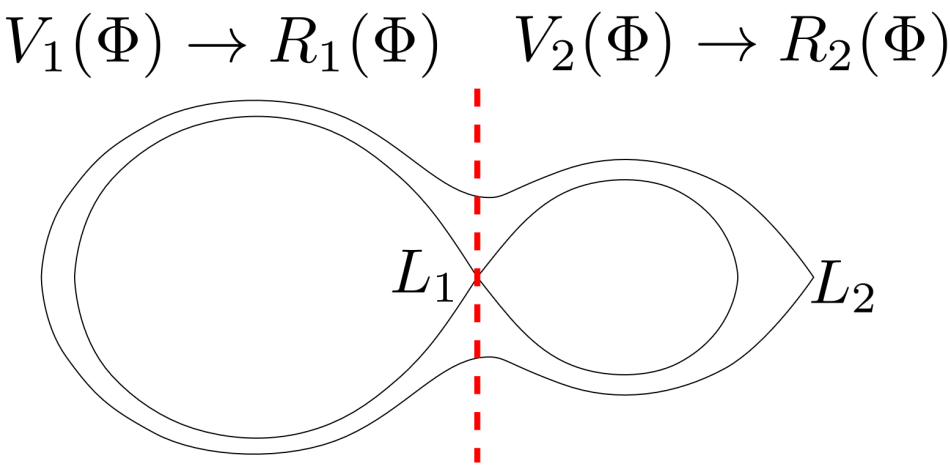

Figure 3.1: Meridional cross-section of two equipotential surfaces – crossing the inner (L_1) and the outer (L_2) Lagrangian point – of an over-contact binary. The system is divided in two separate volumes by a plane crossing L_1 (here: indicated as the red dashed line). Each volume is associated with a corresponding volume equivalent radius, as described in section 3.2. The figure is taken from Marchant, 2018.

unique equipotential surface". Hence, stellar quantities are calculated in one dimension along a volume equivalent radius under assumption of shellularity (instead of calculating along a Euclidean radius under assumption of spherical symmetry).

The amount of mass transferred from one component to the other basically ensures both stellar surfaces to lie on the same equipotential surface. The quantified amount of mass transfer is described in detail by Marchant, 2018.

3.3 Initialization

Calculating a new grid of around 2700 binary models, as done in Menon et al., 2021, would undoubtedly be a reliable method to see the direct influence of different mixing parameters on the population of contact binaries at a mass ratio close to one, but the effort would be beyond the scope of this work. Instead, only a few models with different mixing parameters are calculated, whose results are processed in order to give a hint to the influence of the parameters to the mass-ratio distribution in an eventual grid.

Menon et al., 2021 gave two example models to illustrate the major evolutionary channels in their grids. In this thesis, the example named "System 2" is used as a starting point. Hence, all models also have the same initial masses ($M_1 = 14.4\,\mathrm{M}_\odot, M_2 = 11.6\,\mathrm{M}_\odot$) and the same initial period ($P_\mathrm{i} = 1\,\mathrm{d}$), consistently with "System 2". All the models are terminated analogously to Menon et al., 2021, either at L_2 overflow (because they are expected to merge) or at the end of the main sequence. As a first step, the model is recalculated to ensure that the results can be reproduced. After that, twelve detailed binary models are calculated that are basically a recalculation with modified mixing parameters (α_ov, α_sc and B).

In the following, the concrete choice of mixing parameters is presented (values used in Menon et al., 2021 are in bold).

- **Semiconvection efficiency parameter** $\alpha_\mathrm{sc} \in \{10^{-4},\ \mathbf{1},\ 10^{10}\}$
  In Menon et al., 2021 a semiconvection efficiency parameter of $\alpha_\mathrm{sc} = 1.0$ was included with reference to the work of Langer, Fricke and Sugimoto, 1983 and Schootemeijer et al., 2019. The effect of α_sc on the mass ratio evolution should not only be statistically noticeable in a grid, but rather it should be clearly visible in individual models. Therefore, two extreme cases ($\alpha_\mathrm{sc} = 10^{-4}, 10^{10}$) are chosen.

- **Step overshooting parameter** $\alpha_\mathrm{ov} \in \{0,\ 0.15,\ \mathbf{0.335}\}$
  In Menon et al., 2021 the step overshooting parameter of α_ov= 0.335 was included with reference to the work of Brott et al., 2011. As mentioned in section 3.1, overshooting has to be constrained if the effect of semiconvection is taken into account, otherwise it erases the composition gradient in areas where semiconvection would otherwise have occurred. The first approach chosen here is to completely switch off overshooting ($\alpha_\mathrm{ov} = 0$). The next step is to limit the extent of the overshooting region ($\alpha_\mathrm{ov} = 0.15$).

- **Ledoux term** $B \in \{\mathbf{-},\ 10^{-20},\ 0.1\}$
  In Menon et al., 2021 the Ledoux term was not included, there was no threshold for the composition gradient, beyond which overshooting is halted. Next to reducing α_ov, including the Ledoux term B is a second tool for constraining overshooting. For this thesis, a very strict threshold of ($B = 10^{-20}$) and a more relaxed one ($B = 0.1$, following Marchant, 2018, section 5.1.2) is chosen.

The concrete combination of mixing parameters that is chosen for this thesis can be extracted from table 3.1. One may notice that the variation in the Ledoux term B is not evenly distributed. On the one hand, a threshold for the composition gradient to halt overshooting is not needed, if there is no overshooting at all ($\alpha_\mathrm{ov} = 0$). On the other hand, reducing α_ov and B are handled as two different tools for constraining overshooting. Because of that, there is no variation in B any more as soon as α_ov is constrained to 0.15.

Table 3.1: Overview of the combination of the initial parameters for which models have been calculated. Model 7 in this table is a recalculation of the "System 2" Model in Menon et al., 2021.

#	$\alpha_{\rm ov}$	$\alpha_{\rm sc}$	B
1	0	10^{-4}	-
2		1	
3		10^{10}	
4	0.335	10^{-4}	10^{-20}
5			0.1
6			
7		1	-
8			10^{-20}
9			0.1
10		10^{10}	
11	0.15	10^{-4}	
12		1	
13		10^{10}	

3.4 Mean Observable Mass Ratio

In Menon et al., 2021 a probability distribution of finding a system in given bins of mass ratio was calculated by taking each system from their grid and determining the time it spends in contact at that ratio bin (for details, cf. section A2 in their paper).

For the purpose of this thesis, a non-statistical single parameter per binary model is needed that makes the effect of the chosen parameters to the observed mass ratio during contact comparable. The following describes how this *mean observable mass ratio* was determined.

MESA calculates the binary evolution in discrete steps. Each step is assigned a model number. Among others, the mass ratio $q = \frac{M_2}{M_1}$ is given for each step, where M_1 is the *initial* more massive and M_2 the initial less massive star. An observer cannot distinguish between the initial less and the currently less massive star. Therefore, one can define the observable mass ratio $q_{\mathrm{obs}} = \frac{M_2}{M_1}$, where M_1 is the *currently* more massive and M_2 the currently less massive star, with the result that $q_{\mathrm{obs}} \leq 1$.

Just like in Menon et al., 2021, it is defined that the system is in strict (relaxed) contact at the moment t, if the condition

$$\frac{R\,(t)}{R_{\mathrm{RL}}\,(t)} \geq c \tag{3.2}$$

holds for $c = 1$ ($c = 0.9$) – for the primary as well as for the secondary at the same time. R is the radius of the star and R_{RL} is the radius of its Roche lobe. During evolution, a binary may undergo more than one contact period.

The mean observable mass ratio during contact

$$\bar{q}_{\mathrm{obs}} = \frac{\sum_{i=1}^{N} \int_{a_i}^{b_i} q_{\mathrm{obs}}\,(t)\,\mathrm{d}t}{\sum_{i=1}^{N} (b_i - a_i)} \tag{3.3}$$

is calculated via averaging over time, where N is the amount of contact eras, and a_i (b_i) is the moment in time, where contact period i starts (ends). The integral is numerically approximated via the trapezoidal rule.

For this thesis, $\bar{q}_{\mathrm{obs}}$ for strict and for relaxed contact are of interest. The smaller $\bar{q}_{\mathrm{obs}}$, the less likely it will be to find the binary system during contact at a mass ratio close to 1.

3.5 Equal Mass Quotient

In order to ensure comparability to the results of Menon et al., 2021, there is a second parameter calculated for each model, next to the mean observable mass ratio $\bar{q}_{\mathrm{obs}}$ (cf. section 3.4) that is intended to give the portion of the contact phase that is spent at a mass ratio close to one. For this purpose, the

"equal mass quotient"

$$f = \frac{\tau_q}{\tau} \tag{3.4}$$

is used, where τ is the total amount of time spend on contact (either strict or relaxed as defined in eq. 3.2) and τ_q is the time spent at an observable mass ratio interval $0.95 \leq q_{obs} \leq 1.0$ during contact. As a consequence, there are two values of f for every model, one for strict and one for relaxed contact. This parameter is comparable to the last bin in the $q_{contact} - H_{contact}\,(\Delta q)$ - diagram in Menon et al., 2021, figure 9.

3.6 Rejuvenation Quotient

In order to make a statement about the degree of rejuvenation of a convective core (at a time t), the rejuvenation quotient

$$R = \frac{M_{cc,bin}}{M_{cc,single}} \tag{3.5}$$

is used. $M_{cc,bin}$ is the mass of the convective core of the chosen binary component (either the primary or the secondary star) at chosen point in time. $M_{cc,single}$ is the mass of the convective core of a single star with the same total mass M_{tot} as well as the same central hydrogen mass fraction X_c.

The higher R, the more rejuvenated is the convective core of the binary component. $R = 1$ means that the extent of the convective core is the same as if it was a single star with its current total mass undergoing core contraction due to nuclear burning. For this thesis, R before and after an episode of mass transfer is of interest for each star, since R is not expected to change when mass transfer does not occur. The following describes how exactly dividend and divisor of R are determined.

$M_{cc,bin}$ is the mass of the convective core at the chosen points in time inclusively overshooting. Overshooting needs to be taken into account because the extent of the overshooting region is varied for the different models.

An exact way of determining $M_{cc,single}$ would be to create a detailed single star evolution model with MESA for each R – with the same total mass and the same mixing parameters the corresponding model has. Because the time required for this method goes beyond the scope of this work, a more analytical way of estimating $M_{cc,single}$ is chosen: Figure 3.2 shows the mass of the convective cores at zero-age and terminal-age main sequence for different total masses in a grid calculated by Marchant, 2018. The following describes an example to determine $M_{cc,single}$ for a star with $M_{tot} = 15 M_\odot$ and $X_c = 0.4$. As a first step, a pair of values $(M_{cc,ZAMS}, M_{cc,TAMS})$ is extracted from fig. 3.2, here marked as red points with labels (A, B). The central hydrogen mass fraction is assumed to start at ZAMS with $X_c = 0.7$ and to end at TAMS with $X_c = 0$. As the core contracts with decreasing X_c, the extracted pair of values is assumed to define a straight line in a X_c - M_{cc} - diagram, as depicted in fig. 3.3. Consequently, $M_{cc,single}$ is calculated via the line equation at the given point $X_c = 0.4$, here resulting to $M_{cc,single} = 5\,M_\odot$.

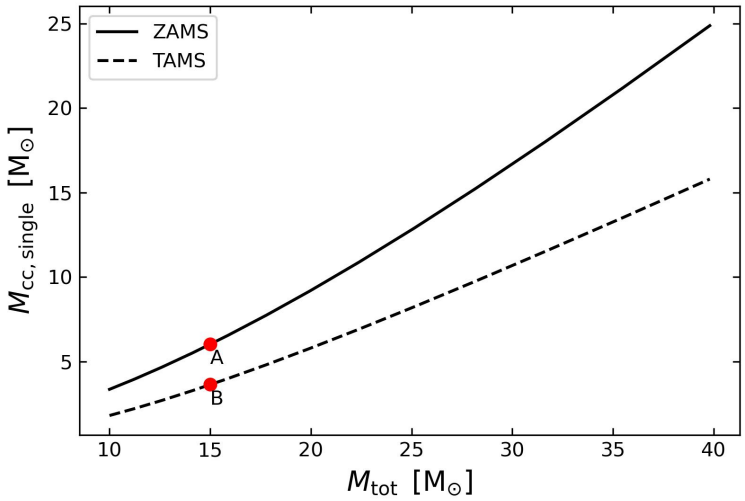

Figure 3.2: Convective cores of single stars. M_{tot} is the total mass of a single star, $M_{cc,single}$ is the mass of its convective core (without overshooting) at ZAMS (zero-age main sequence) and TAMS (terminal-age main sequence), respectively. The source of data is provided by Schürmann et al., in prep. It is based on a grid of detailed binary models calculated by Marchant, 2018 (chapter 5) with $\alpha_{sc} = 0.01$, $\alpha_{ov} = 0.335$ and $B = 0.1$. Points marked in red are intended to show the exemplary reading of a pair of values (see text in section 3.6).

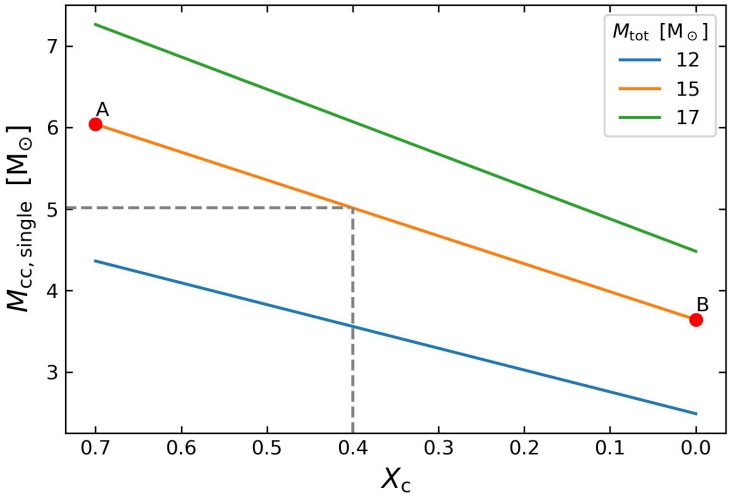

Figure 3.3: Retracting convective cores of single stars with different total masses M_{tot}. The straight lines in this figure are not numerically calculated with MESA but derived from pairs of values in fig. 3.2. Points A and B also correspond to points A and B in fig. 3.2. The gray dashed lines indicate an exemplary reading of a convective core mass M_{cc} for a given central hydrogen mass fraction X_c (see text in section 3.6).

CHAPTER 4

Results

4.1 Example Models

A recalculation of the binary evolution model corresponding to the parameter setup of the *System 2* example in Menon et al., 2021 shows that their results can be reproduced: Right panels in figure 4.1 coincide with the System 2 panels of figure 1 in their paper. The Kippenhahn diagrams in figure 4.1 show a broad overshooting region, nearly constant in extent, consistent with the rather large step overshooting parameter $\alpha_{\mathrm{ov}} = 0.335$.

The binary models created for this thesis can be divided in three types, depending on their appearance – more precisely, depending on the total mass evolution of their components. In the following, three example models are used to illustrate the characteristics of the from now on so-called type A, B and C evolution.

Systems following the type A evolution behave like "System 2" in Menon et al., 2021 that was used as a starting point model for this thesis (see section 3.3). System A in figure 4.2(a) represents type A evolution: One fast mass transfer episode on thermal timescale occurs after a while (here at about 3.6 Myr), followed by a short detached phase, until mass transfer from the less massive to the more massive component starts on the nuclear timescale due to a semi-detached configuration, finally leading to the last episode of mass transfer on a nuclear timescale, where mass ratio approaches unity.

Exactly like system 2 in figure 4.1, system A in figure 4.2(a) starts with a broad overshooting region due to α_{ov}= 0.335. The Secondary Kippenhahn of system A shows the effect of the additionally implemented Ledoux term B in this model: After the first mass transfer on thermal timescale, the overshooting region encounters the composition gradient the convective core left behind, and is therefore constrained to a negligibly small extent. Comparing the following mass transfer phase from the less massive to the more massive star in the secondary Kippenhahn of system A with the corresponding phase of system 2, it turns out that overshooting in system 2 straightens the composition gradient where otherwise semiconvection would have occurred. The Ledoux term also has an effect on the primary star: Comparing the last mass transfer episode on nuclear timescale of system 2 (at around $t = 7$ Myr) with system A (at around $t = 6$ Myr) one can see that also here the extent of the overshooting region is slightly constrained.

The effect of B on the total evolution of system A is rather small: System A has a slightly shorter lifespan ($\tau_{\mathrm{tot}} = 9.32$ Myr) in comparison to system 2 ($\tau_{\mathrm{tot}} = 9.81$ Myr) due to the less burning material that is available in the convective core. More relevant for this thesis: The final mass ratio of system A is further away from unity in comparison to system 3, but for example it also starts with a mass ratio closer

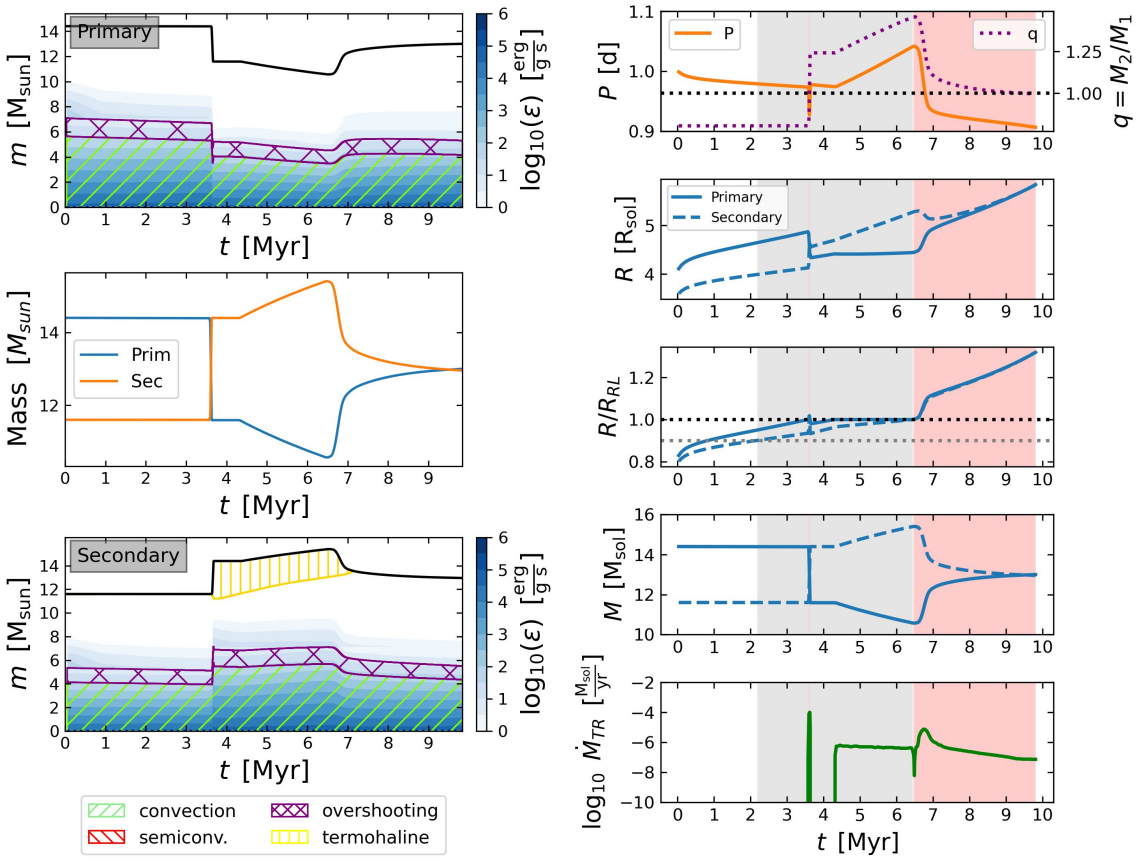

Figure 4.1: A recalculation of the binary model "System 2" from Menon et al., 2021 with initial masses $M_{1,\mathrm{i}} = 14.4$, $M_{2,\mathrm{i}} = 11.6$, an initial orbital period $P_{\mathrm{i}} = 1$ d and the mixing parameters $\alpha_{\mathrm{ov}} = 0.335, \alpha_{\mathrm{sc}} = 1$. There is no Ledoux term B included. The left panels show Kippenhahn diagrams for the primary and the secondary, respectively, together with the total mass evolution of the binary. The panels on the right have the same pattern as figure 1 in Menon et al., 2021. The color scheme is reassigned here: Red background shades indicate strict contact phases ($R/R_{\mathrm{RL}} \geq 1$ for both components), gray shades indicate near-contact phases ($0.9 \leq R/R_{\mathrm{RL}} < 1$ for both components). Relaxed contact phases are the sum of red and gray phases. The model terminated because of L2 overflow.

to unity at the beginning of the last mass transfer on nuclear timescale (at arount $t = 6\,\mathrm{Myr}$).

Systems following type B evolution (represented by system B in figure 4.2(b)) are very similar to type A: Exactly like type A systems, they have one mass transfer (MT) on thermal timescale, a semi-detached phase and a final mass transfer phase on nuclear timescale. The only difference to type A: During nuclear timescale MT (in system B starting around $t = 6.3\,\mathrm{Myr}$), the mass ratio q is not approaching, but oscillating around unity. Comparing the Kippenhahn diagrams of system B in figure 4.2(b) with system A in figure 4.2(a), the rather thin overshooting region sticks to the eye, agreeing with the smaller overshooting parameter $\alpha_{\mathrm{ov}} = 0.15$ that is implemented in this model. The effect of the Ledoux term B is visible in the Kippenhahn diagrams analogous to system A, this time even allowing for a second region of semiconvection (see primary Kippenhahn of system B at the beginning of contact on nuclear timescale). Finally, system B has a smaller lifetime ($\tau_{\mathrm{tot}} = 9.06\,\mathrm{Myr}$) than system A ($\tau_{\mathrm{tot}} = 9.32\,\mathrm{Myr}$) as expected from the smaller overshooting parameter providing less burning material for the core.

Models evolving like system C (figure 4.2(c)) stand out in comparison to type A and B evolution: Type C systems avoid contact on nuclear timescale at all. Exactly like Systems A and B they start with a contact on thermal timescale (here at around $t = 3.2\,\mathrm{Myr}$), followed by a detached and a semi-detached phase. But instead of entering a contact on nuclear timescale, they enter a second contact on thermal timescale (here around $t = 6.7\,\mathrm{Myr}$). The sequence - thermal timescale contact, detached and semi-detached configuration - repeats at least one time before the model is terminated.

A look at the corresponding Kippenhahn diagrams of system C shows that there is no overshooting at all (as expected from the initial mixing parameter $\alpha_{\mathrm{ov}} = 0$). That also allows for much more semiconvection to occur – not only at the semi-detached or contact configurations as in systems A and B, but also in the initial detached configuration: The primary has small regions of semiconvection as the convective core retracts (starting from $t = 1\,\mathrm{Myr}$).

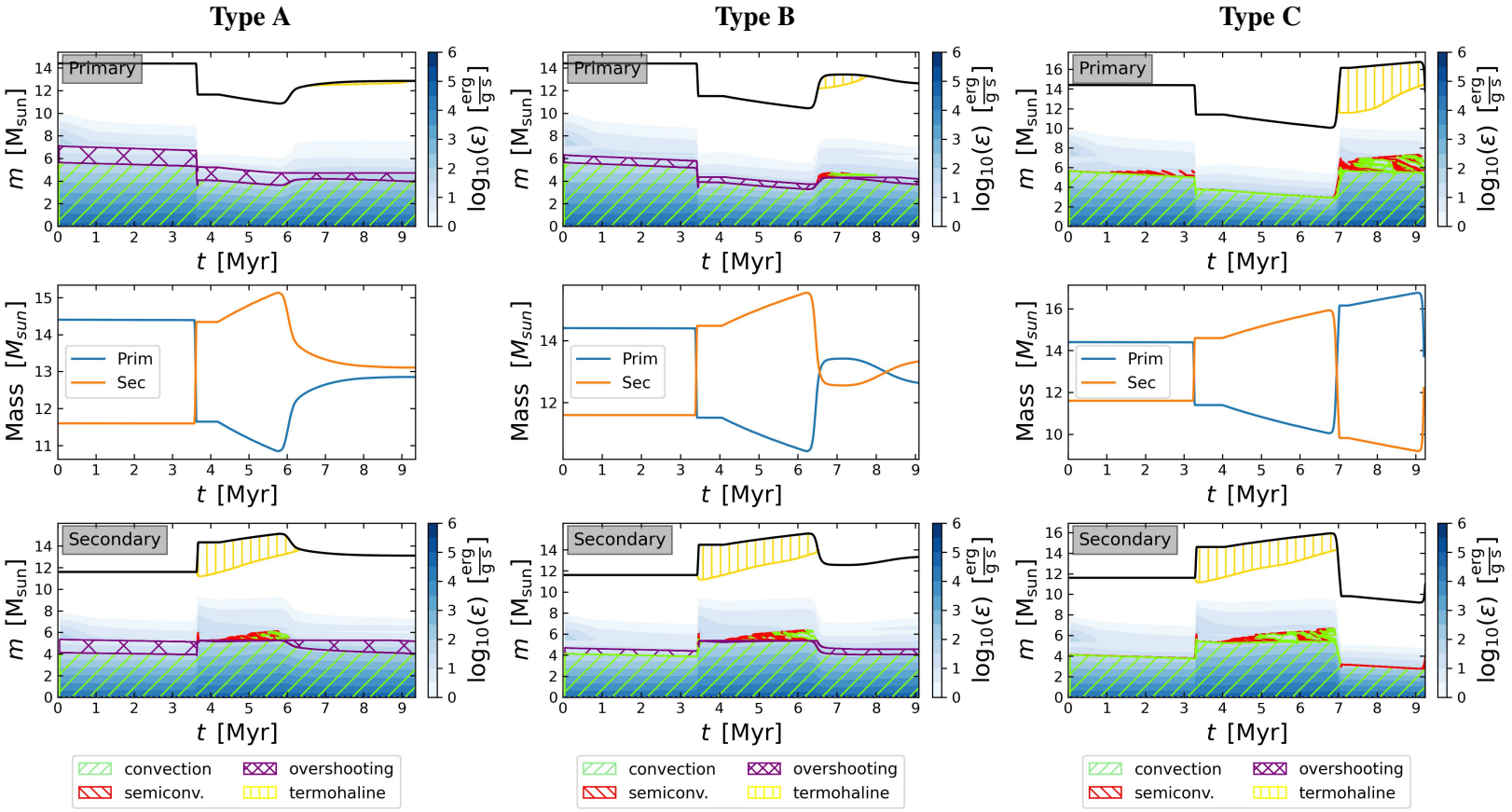

(a) "System A"
model 3 – α_{ov} = 0.335

(b) "System B"
model 7 – α_{ov} = 0.15

(c) "System C"
model 11 – α_{ov} = 0

Figure 4.2: Three selected binary evolution models representing their type of total mass evolution of their components as described in section 4.1 with α_{sc}= 1 and B = 0.1 (System C has no B implemented as there is no overshooting). Every column features Kippenhahn diagrams for the primary and the secondary, respectively, together with the total mass evolution of the binary components. The hatching shows regions of different mixing processes (as indicated) and blue shades point out nuclear energy generation. Model numbers in each caption correspond to table 4.1.

4.2 System Properties

In all models, there are certain recurring evolutionary phases: contacts on thermal and nuclear timescale, as well as semi-detached phases. In the following, the example models already introduced in section 4.1 are used to examine these phases in more detail. For this purpose, figure 4.3 deals with the system properties of the example models A, B and C, following the style of Menon et al., 2021, Figure 1.

Mass transfer on thermal timescale occurs as the first episode of mass transfer for every model in this thesis (system A: around 3.5 Myr, system B: 3.3 Myr, system C: 3.2 Myr). Type C models do have more than one thermal timescale contact phases, in system C there are two more of them (around 6.7 Myr and 9.1 Myr). Both stellar components overflow their respective Roche lobes ($\frac{R}{R_{\mathrm{RL}}} \geq 1$). Thus, thermal timescale mass transfer occurs during strict contact (corresponding to the narrow red shades in fig. 4.3). The more massive star loses its mass M and shrinks in radius R rapidly, while the lower mass star does the opposite. A characteristic feature of the thermal timescale mass transfer is the drop in orbital period P: P reaches a local minimum when mass ratio q has reached unity ($q = 1$), and recovers again as soon as q inverses, as expected from considerations of conservation of total angular momentum (cf. sec. 2.5). The orbital separation a behaves similar to the orbital period (Kepler's third law $P^2 \propto a^3$). When P recovers, the orbital separation rises again, both stars finally detach and mass transfer is stopped.

Mass transfer from the less massive to the more massive star does always happen on a nuclear timescale in the calculated models, as expected from theory (sec. 2.5). Thermal timescale mass transfer and the subsequent detached configuration is always followed by this kind of mass transfer, as soon as the now less massive star fills its Roche lobe again (system A: 4.2 Myr, system B: 4.0 Myr, system C: 4.0 Myr and 7.3 Myr). The system stays in a detached configuration ($\frac{R}{R_{\mathrm{RL}}} \geq 1$ only for the donor) as orbital separation (and period) rises. The semi-detached configuration ends, when the currently more massive star fills its Roche lobe - leading to a next contact phase (either on thermal or nuclear timescale).

Systems following evolution type A and B exhibit a mass transfer phase on *nuclear* timescale during contact at the end of the simulations (system A: 5.8 Myr, system B: 6.2 Myr). They enter this phase by leaving the semi-detached configuration (when the more massive acceptor fills its Roche lobe), exactly like system C, when it enters a second contact on *thermal* timescale (around 6.8 Myr). The only difference is that systems A and B remain in contact, system C breaks contact after approximately 0.2 Myr. The cause that determines whether stars stay in contact on the nuclear timescale or break it off by detaching is unexplored yet and requires further research.

A closer look at the evolution of mass transfer rates $\dot{M}_{\mathrm{TR}}$ during contact on nuclear timescale for different types of evolution may suggest a connection: The mass transfer rate during contact of system B (fig. 4.3(b)) shows two "hills" indicating an inversion of mass transfer that is the reason for the "oscillation in total mass" that is characteristic for type B. The first hill and the beginning of a second hill is also visible during contact on nuclear timescale in system A (fig. 4.3(a)), with the only difference that the first hill is more extended in time and the initial mass transfer rate at contact (around 6 Myr) is not high enough to inverse the mass ratio. The comparison of all three systems shows that the extent of the overshooting region can have a considerable impact on the period of contact at nuclear timescale: It can affect the frequency and the amplitude of mass ratio oscillation during contact, or even whether the system avoids the contact period at all.

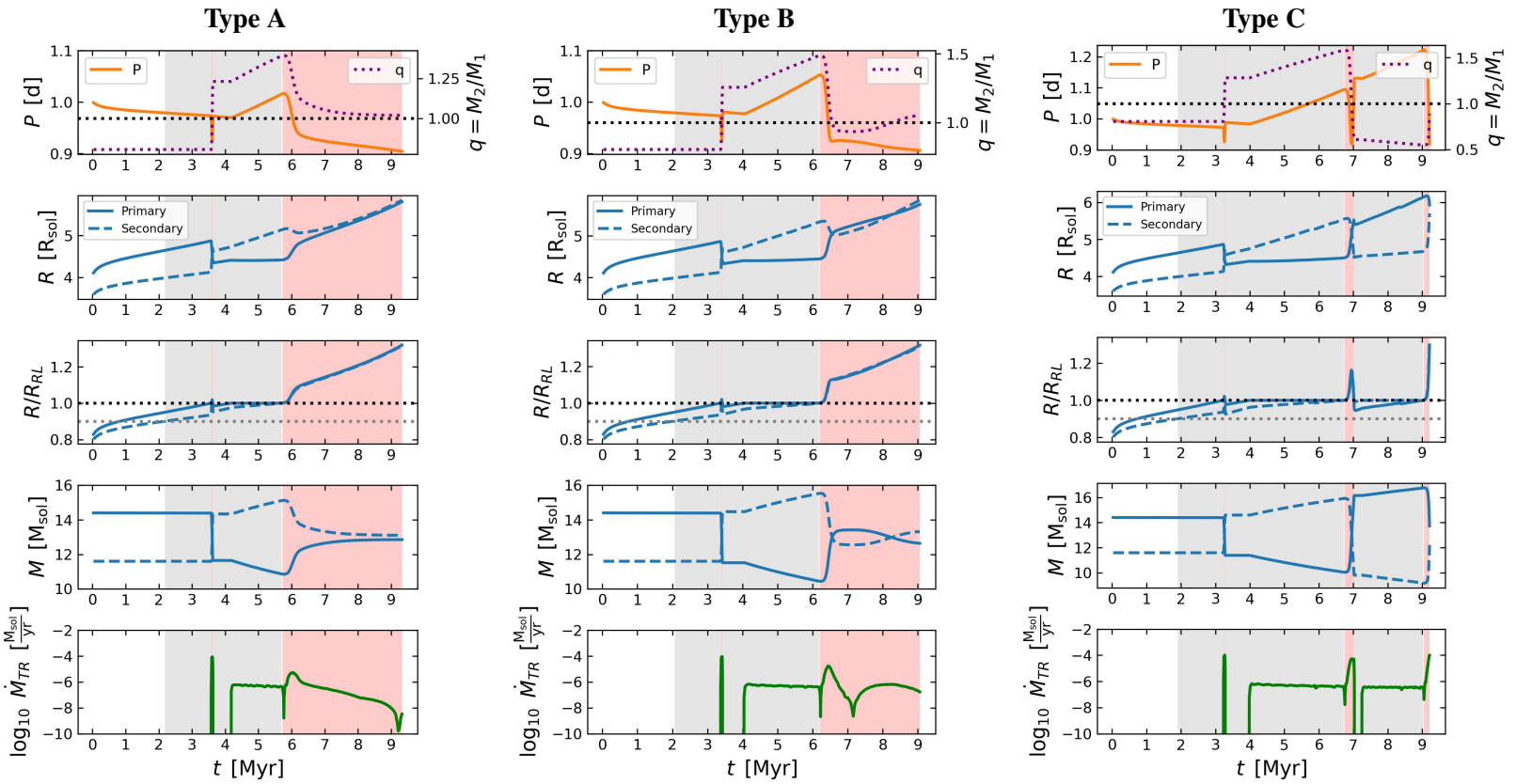

(a) "System A"
model 3 – $\alpha_{ov} = 0.335$

(b) "System B"
model 7 – $\alpha_{ov} = 0.15$

(c) "System C"
model 11 – $\alpha_{ov} = 0$

Figure 4.3: Detailed system properties of the three example models depicted in figure 4.2, following the style of Menon et al., 2021, Figure 1. Again, α_{sc}= 1 and $B = 0.1$ (System C has no B implemented as there is no overshooting). Model numbers in each caption correspond to table 4.1. The first row features the period (left axis) and the mass ratio evolution (right axis). The other panels exhibit the total radius R, the relative Roche lobe overflow R/R_{RL}, the total mass M of the components and the rate of mass transfer $\dot{M}_{TR}$. Red background shades indicate strict contact phases ($R/R_{RL} \geq 1$ for both components), gray shades indicate near-contact phases ($0.9 \leq R/R_{RL} < 1$ for both components).

4.3 Impact of Semiconvection

This section is intended to give an overview of the impact of semiconvection efficiency to the overall mass ratio evolution for different extents of the overshooting region ($\alpha_{ov} = 0.335$ in figure 4.4, $\alpha_{ov} = 0.15$ in figure 4.5 and $\alpha_{ov} = 0$ in figure 4.6). Each figure collates three different efficiencies of semiconvection ($\alpha_{sc} = 10^{-4}, 1, 10^{10}$).

Beginning with $\alpha_{ov} = 0.335$, it stands out that semiconvection exclusively plays a role during the semi-detached and the preceded detached phase in the secondary star (see secondary Kippenhahn diagrams in fig. 4.4 between $3.8\,\mathrm{Myr} \lesssim t \lesssim 6\,\mathrm{Myr}$). Consequently, modifying the efficiency of semiconvection via α_{sc} foremost has an impact on this stadium: The lifetime of the semi-detached phase increases as α_{sc} increases (until $\approx 5.8\,\mathrm{Myr}$ in fig. 4.4(a), until $\approx 6\,\mathrm{Myr}$ in fig. 4.4(b) and until $\approx 6.4\,\mathrm{Myr}$ in fig. 4.4(c)). The mass ratio at the end of semi-detached configuration rises with the lifetime of this phase (and also with α_{sc}) as mass transfer rate stays constant during semi-detached configuration (see constant slope of component mass evolution during the semi-detached phases in the second row of fig. 4.4).[1]

The lifetime of the detached phase is ruled by the radius evolution of the acceptor (here the primary) as described in section 4.2: The phase ends as soon as the acceptor fills its Roche lobe – leading to a next contact phase. Comparing the secondary Kippenhahn panels in figure 4.4 reveals the reason for a different secondary radius evolution: A minor efficiency of semiconvection leads to a well-defined semiconvective layer that operates as separation between the convective core and another convective layer that grows in mass as the secondary gains mass during the semi-detached configuration (red layer in the secondary Kippenhahn of fig. 4.4(a)). This separation effectively prevents the enrichment of the core with the burning material hydrogen, and therefore leads to a nuclear evolution that is unaffected by the mass gain. With an increased efficiency of semiconvection ($\alpha_{sc} = 1.0$), the efficiency is high enough to create some convective zones in the otherwise semiconvective layer as the composition gradient is smoothed (cf. fig. 4.4(b) and sec. 2.3 for theory). Efficiency is expected to be high enough to enrich the convective core with hydrogen. The core is rejuvenated as it has more burning material, the radius increases slower, and it takes longer to fill the secondary Roche lobe. With $\alpha_{sc} = 10^{10}$, there is no direct layer of semiconvection visible in the secondary Kippenhahn diagram of fig. 4.4(c). Here, semiconvection efficiency is high enough to immediately smooth the composition gradient that would otherwise constrain the overshooting region (via B), the convective core effectively grows after mass transfer on thermal timescale (around $t = 3.8\,\mathrm{Myr}$), joining with a broad, unconstrained overshooting region – leading to a strong rejuvenation and the most extended lifespan of the semi-detached configuration.

Proceeding to figure 4.5 with $\alpha_{ov} = 0.15$, it stands out that the first contact on thermal timescale happens earlier (around $t \approx 3.4\,\mathrm{Myr}$) than with $\alpha_{ov} = 0.335$ (around $t \approx 3.6\,\mathrm{Myr}$) as expected from the smaller extent of the overshooting region supplying less burning material to the core and leading to an earlier filling of the primary Roche lobe. The semi-detached phase is affected by the efficiency of semiconvection analogously to the case of $\alpha_{ov} = 0.335$: The lifespan of the semi-detached era lasts longer with increasing α_{sc} and leads to a higher mass ratio at the end of the semi-detached configuration.

This time, efficiency of semiconvection has a considerable impact on the mass transfer rate during

[1] The mass transfer rate is constant, since it is up to the nuclear evolution of the Roche lobe filling donor (here the primary).

contact on nuclear timescale: In figure 4.5(a), a minor α_{sc} leads to preventing a type B evolution.

In the case of no overshooting (fig. 4.6), the efficiency of semiconvection has a strong impact on the total lifespan[2] as a higher semiconvection efficiency enriches the core with hydrogen more effectively. Without a present overshooting region, semiconvection occurs throughout the whole evolution, not only constrained to the semi-detached configurations. This is most conspicuous for $\alpha_{sc} = 10^{-4}$ (cf. fig. 4.6(a)): The semiconvective layer constrains the cores of both components effectively so that they retract almost independently of mass transfer, leading to a very short lifespan in comparison to the cases of figures 4.6(b) & 4.6(c) (rejuvenation is prevented, see also section 4.4). Furthermore, α_{sc} affects the amount of contacts on thermal timescale: models in fig. 4.6(a) and 4.6(b) undergo three extended contacts on thermal timescale[3], while the model in fig. 4.6(c) undergoes four of them.

Comprising, semiconvection preferably affects the lifetime of semi-detached phases (for $\alpha_{ov} = 0.335$ semiconvection exclusively occurs during semi-detached phases, for $\alpha_{ov} = 0$ there is no contact on nuclear timescale). In one case, it additionally affects the contact on nuclear timescale for a constrained overshooting $\alpha_{ov} = 0.15$ ($\alpha_{ov} = 0.15$) by changing the evolution type. Constraining overshooting leads to a higher impact of semiconvection – on the total lifetime as well as on the overall total mass evolution (eg. amounts of contacts on thermal timescale).

[2] For the other extents of the overshooting region ($\alpha_{ov} = 10^{-4}, 1$), a higher α_{sc} means a slightly higher lifespan, too, but only less than 0.5 Myr (compare figures 4.4 & 4.5). For $\alpha_{ov} = 0$, the range of α_{sc}enhances the lifespan up to ≈ 3 Myr!

[3] Model number 10 in fig. 4.6(a) ends with an extremely short period of contact. Therefore, it is listed in table 4.1 with $N_{strict} = 4$.

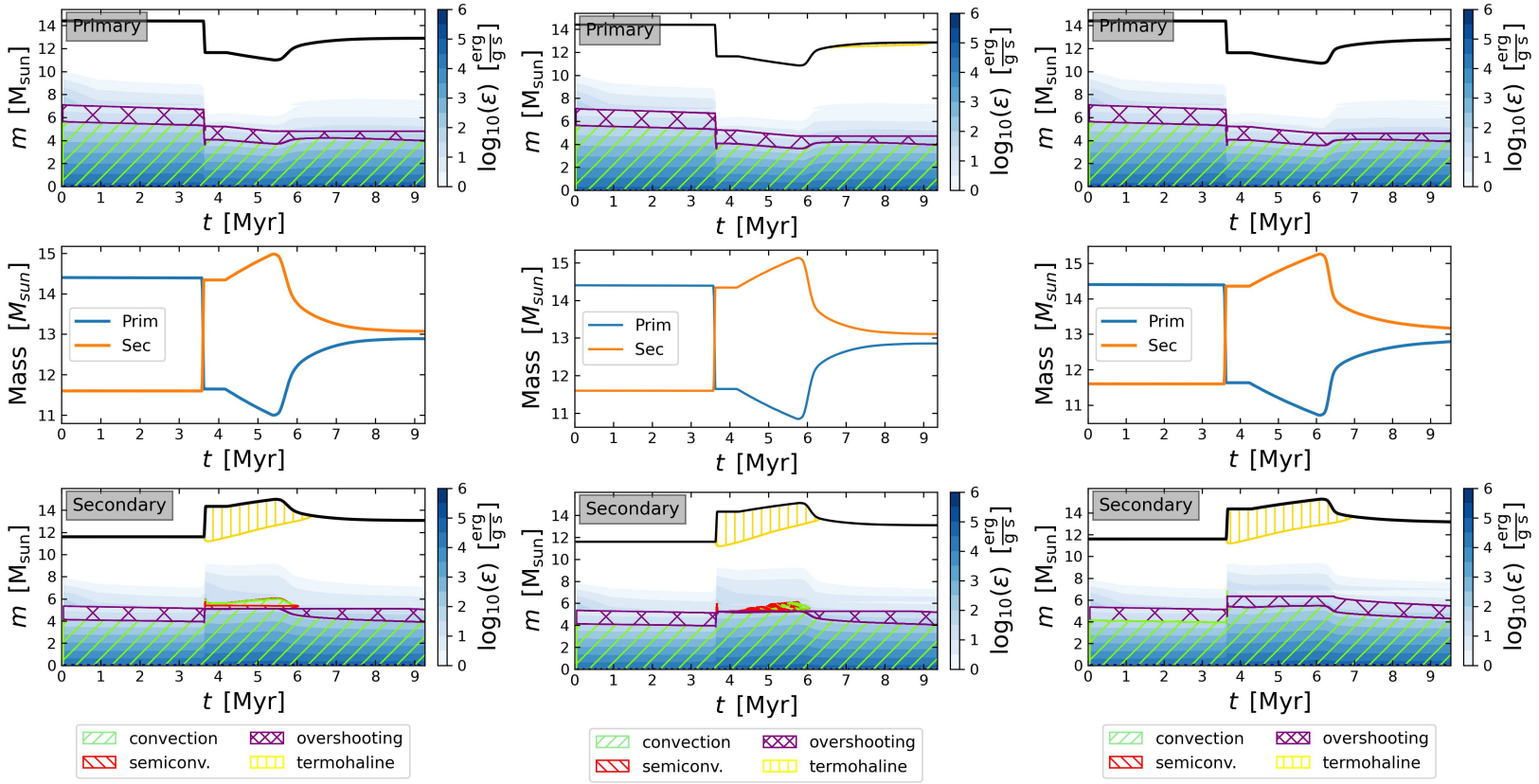

(a) $\alpha_{sc} = 10^{-4}$
model number 1

(b) $\alpha_{sc} = 1.0$
model number 3

(c) $\alpha_{sc} = 10^{10}$
model number 6

Figure 4.4: Three selected binary evolution models showing the impact of semiconvection for a constant $\alpha_{ov} = 0.335$ and $B = 0.1$. Every column features Kippenhahn diagrams for the primary and the secondary, respectively, together with the total mass evolution of the binary components. The hatching shows regions of different mixing processes (as indicated) and blue shades point out nuclear energy generation. Model numbers in each caption correspond to table 4.1.

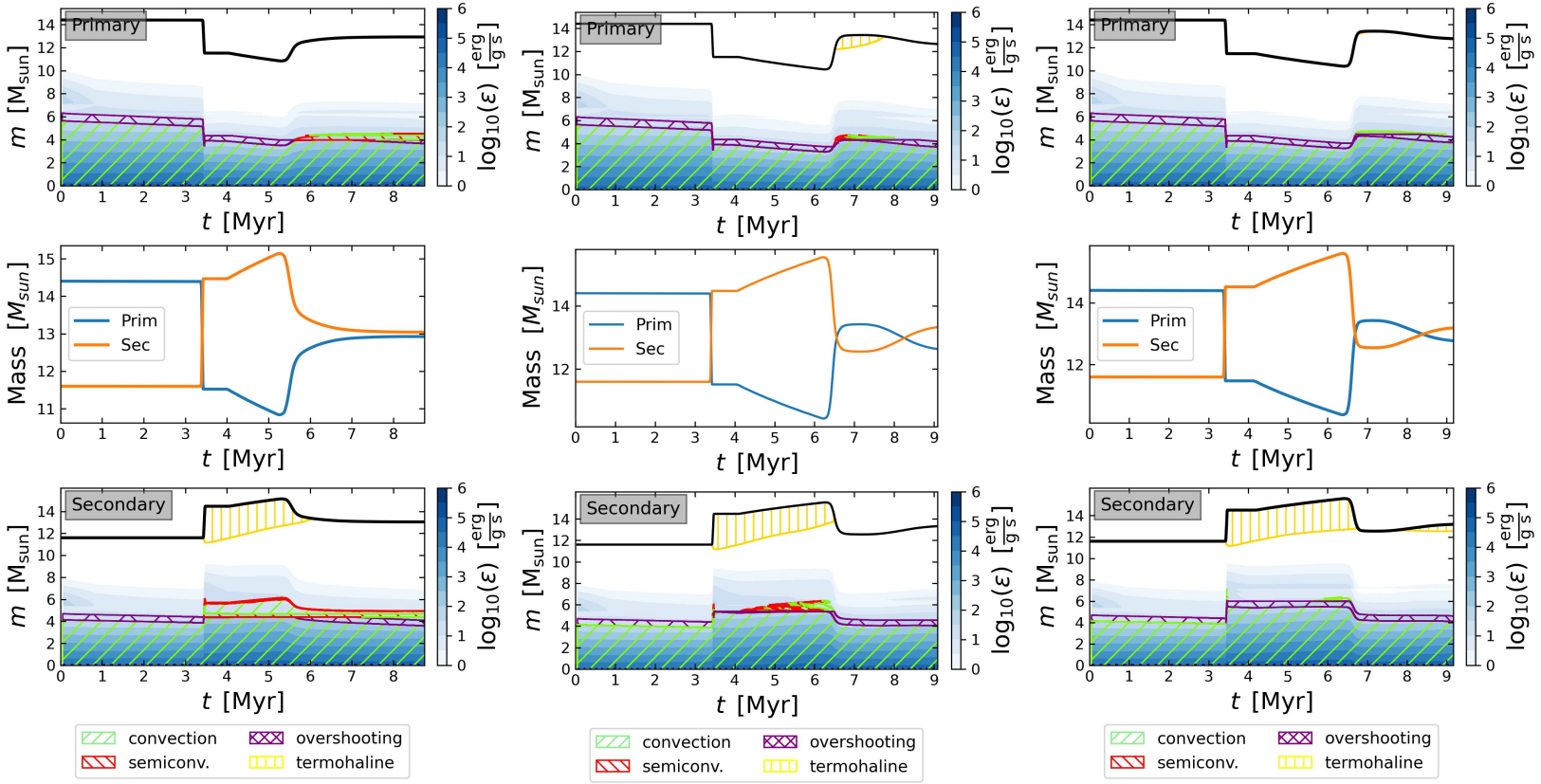

(a) $\alpha_{sc} = 10^{-4}$
model number 2

(b) $\alpha_{sc} = 1.0$
model number 7

(c) $\alpha_{sc} = 10^{10}$
model number 8

Figure 4.5: Three selected binary evolution models showing the impact of semiconvection for a constant $\alpha_{ov} = 0.15$ and $B = 0.1$. Every column features Kippenhahn diagrams for the primary and the secondary, respectively, together with the total mass evolution of the binary components. The hatching shows regions of different mixing processes (as indicated) and blue shades point out nuclear energy generation. Model numbers in each caption correspond to table 4.1.

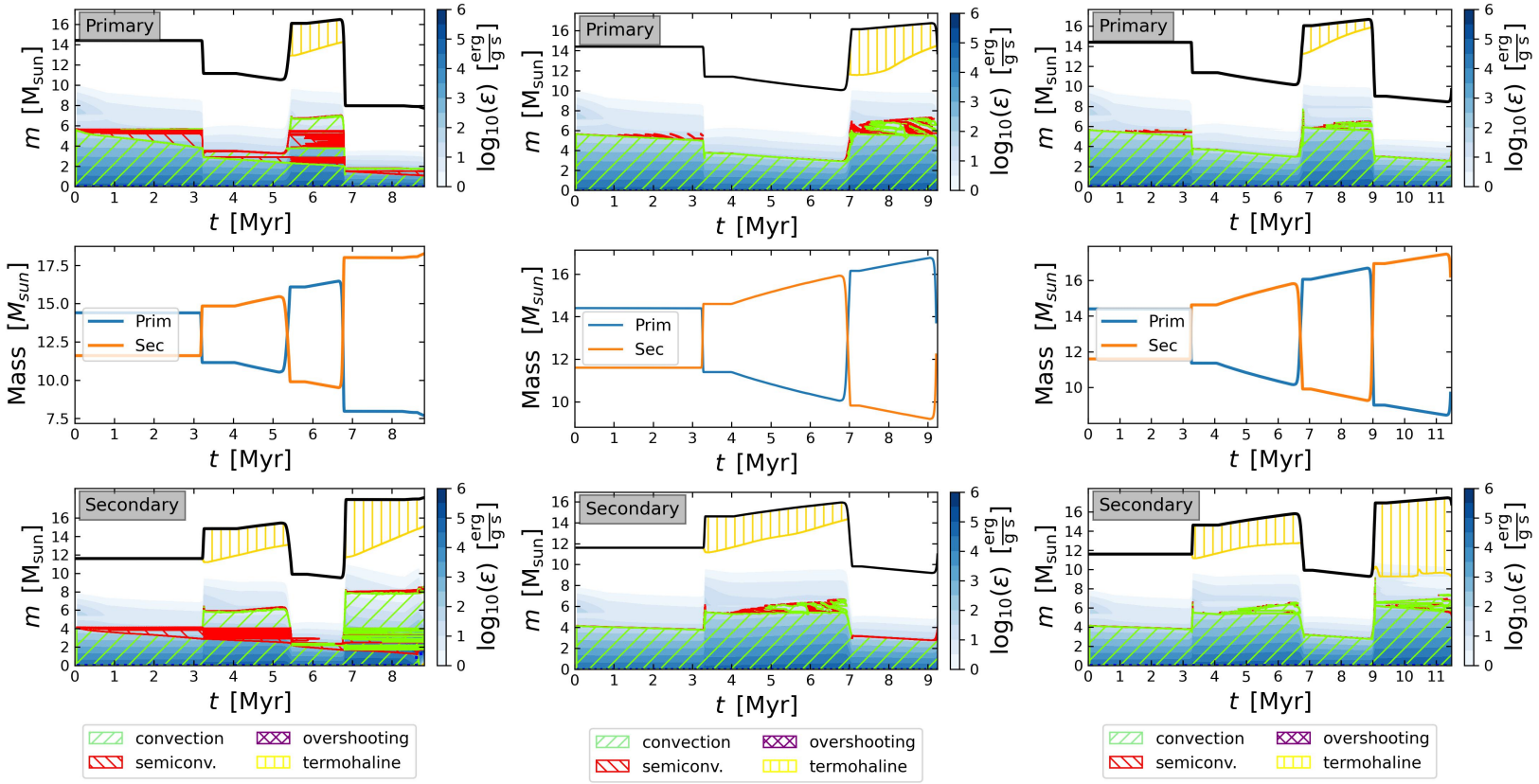

(a) $\alpha_{sc} = 10^{-4}$
model number 10

(b) $\alpha_{sc} = 1.0$
model number 11

(c) $\alpha_{sc} = 10^{10}$
model number 13

Figure 4.6: Three selected binary evolution models showing the impact of semiconvection for a constant $\alpha_{ov} = 0$ (consequently, there is no B included). Every column features Kippenhahn diagrams for the primary and the secondary, respectively, together with the total mass evolution of the binary components. The hatching shows regions of different mixing processes (as indicated) and blue shades point out nuclear energy generation. Model numbers in each caption correspond to table 4.1.

4.4 Rejuvenation

This section investigates the connection between rejuvenation and the observable mass ratio, as assuming a binary with mass ratio $q = 1$ and completely rejuvenated components, both stars are expected to evolve equally, especially their radii would increase simultaneously leading to a stagnation in mass exchange. The following can be put forward as a hypothesis: The more rejuvenation occurs in a binary evolution model, the more probable the binary system will be found at a mass ratio close to one.

The system 2 model in Menon et al., 2021 features instantaneous rejuvenation during mass transfer. Figure 4.7 – left panel, second row – shows the first mass transfer episode for the secondary as an example: The convective core expands (from $5.2\,M_\odot$ to $7.2\,M_\odot$), it is enriched with the less processed material above the core, and the central hydrogen mass fraction rises (from around 0.672 to 0.688). Even the small composition gradient (visualized by the slope of X_H between $5\,M_\odot \leq m \leq 6\,M_\odot$) that was left behind by the contracting convective core is erased after the mass transfer. The star is said to be rejuvenated at this point, because the convective core has gained more burning material. The table for the secondary in fig. 4.7 (left panel) quantizes the rejuvenation via the rejuvenation quotients before ($R_{1A} = 1.26$) and after ($R_{1B} = 1.25$) mass transfer. R does not drop noticeably and $R \geq 1$. The star is not only partially but also completely rejuvenated: The convective core has the same extent as if it was a single star with the same total mass and central hydrogen mass fraction ($R > 1$ at this point, because $M_{cc,single}$ does not account for overshooting, cf. section 3.6). In addition to that, the rejuvenation can be visually affirmed by the Kippenhahn diagrams in fig. 4.1: The extent of the convective core (inclusively the overshooting region) grows and shrinks going along the change in total mass of the star.

In contrast to the grid in Menon et al., 2021, the models calculated in this thesis often show a reduced or even an avoided rejuvenation. The most extreme case of an avoided rejuvenation is given in figure 4.7 (right panel). The hydrogen profiles around the first episode of mass transfer (second row) serves again as an example for the rejuvenation processes, in a direct comparison to the left panel: The extent of the convective core (around $3\,M_\odot$) stays the same before and after mass transfer. No additional hydrogen is mixed into the core, the hydrogen mass fraction X_H even decreases (from around 0.649 to 0.644), as expected due to nuclear burning. Concerning the quantization of rejuvenation (tables in the third row), it stands out that the rejuvenation quotient R is almost monotonically decreasing in time, indicating an avoided rejuvenation during the whole binary evolution. This even becomes impressively clear in the light of the Kippenhahn plots in fig. 4.8 (left panel), where the convective cores of both components retract almost independently of mass transfer. Furthermore, the Kippenhahn diagrams show the cause for the avoided rejuvenation for this model: Layers with a composition gradient (left behind by the retracting core) act as an efficient boundary constraining the extent of the convective core. The small efficiency of semiconvection ($\alpha_{sc} = 10^{-4}$), as well as the absence of overshooting, lead to a preservation of the composition gradients.

Instead of comparing hydrogen profiles for each model (as done before for two extreme cases of (no) rejuvenation), the following is intended to give an overall picture of rejuvenation in all calculated models by evaluating only the set of rejuvenation quotients R (for each binary evolution model, there is a set of calculated R analogously to the tables in fig. 4.7). Figure 4.9 shows all determined values for R and their assigned observable mass ratios q_{obs} the system has at that point in time. Evolutionary lines in this diagram collectively start around $q_{obs} = 0.8$ (marked with the letter A for each highlighted model), but with different degrees of rejuvenation. This indicates the beginning of the first episode of

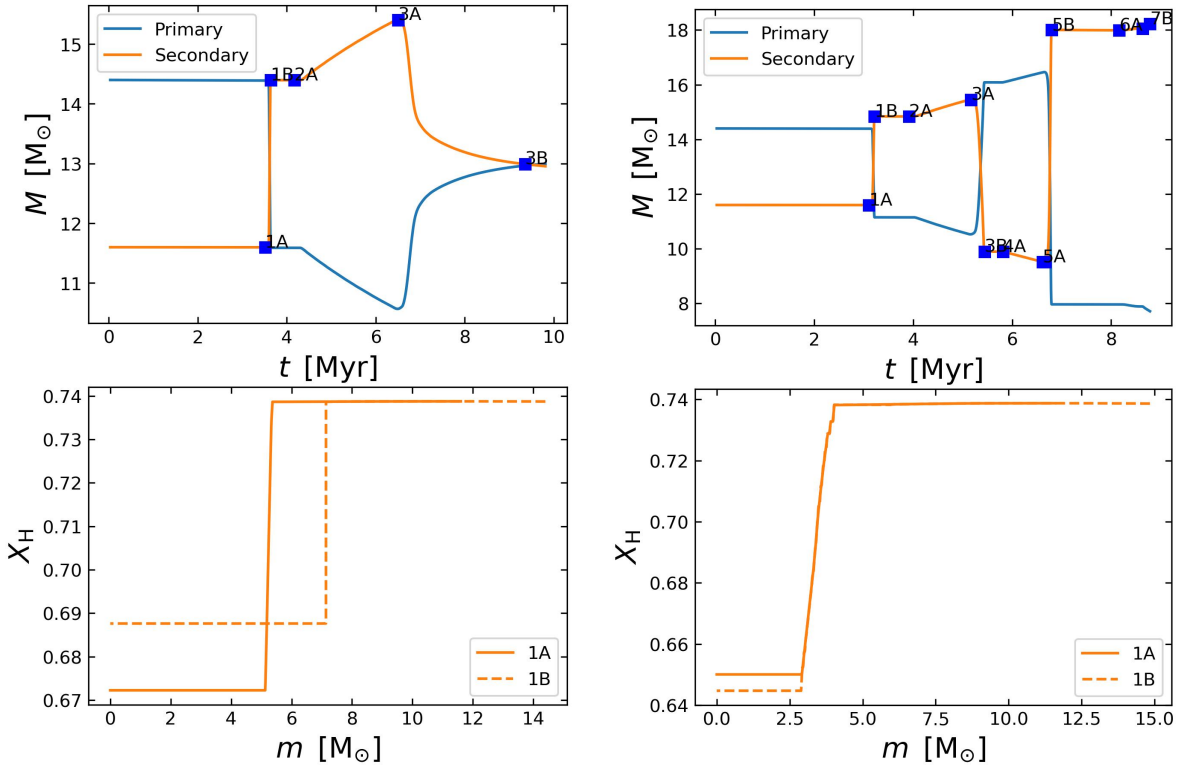

Primary		
#	A	B
1	1.22	1.24
2	1.31	1.35
3	1.35	1.26

Secondary		
#	A	B
1	1.26	1.25
2	1.22	1.20
3	1.20	1.29

Primary		
#	A	B
1	0.71	0.78
2	0.74	0.74
3	0.73	0.38
4	0.38	0.36
5	0.36	0.58
6	0.48	0.47
7	0.46	0.45

Secondary		
#	A	B
1	0.71	0.5
2	0.49	0.45
3	0.45	0.76
4	0.70	0.62
5	0.62	0.25
6	0.25	0.25
7	0.04	0.00

Figure 4.7: Two extrema of models with rejuvenation (left panel) and without rejuvenation (right panel). The first row gives the mass evolution of the binary components. The points in time marked in blue are chosen so that they frame episodes of high mass transfer ($\dot{M}_{\rm TR} \geq 10^{-7}$ M$_\odot$/yr). The second row shows the hydrogen profiles of the secondary components before (1A) and after (1B) the first episode of mass transfer on thermal timescale. The tables give the rejuvenation quotient (see section 3.6) for each associated point in time. The points in time for the primary are determined analogously to those of the secondary star. The left panel is based on a recalculation of the system 2 model in Menon et al., 2021 with $\alpha_{\rm ov} = 0.335, \alpha_{\rm sc} = 1$ and no B (model 5 in table 4.1). The right panel corresponds to model 10 with $\alpha_{\rm ov} = 0$ and $\alpha_{\rm sc} = 10^{-4}$.

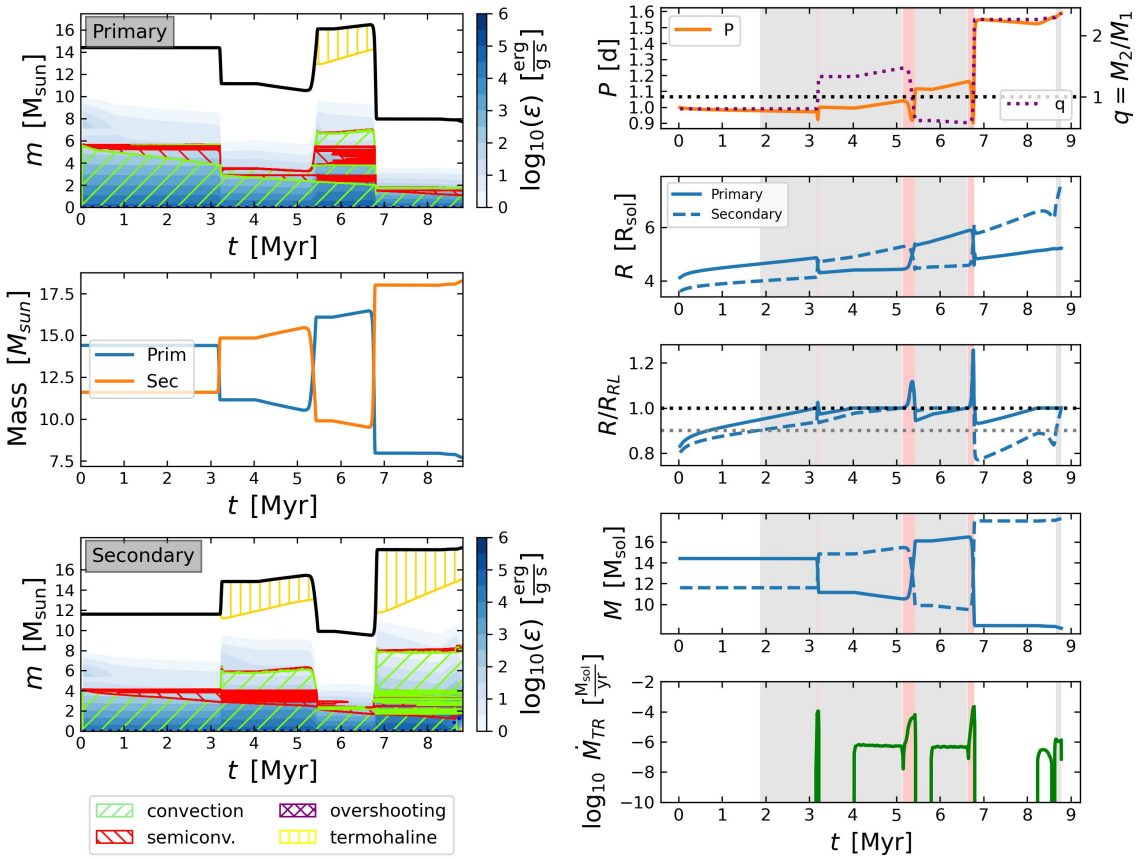

Figure 4.8: An extreme case of a model without rejuvenation. This binary is listed in table 4.1 as model 11 (giving further global system properties and the mixing parameters for this model: $\alpha_{\rm ov} = 0, \alpha_{\rm sc} = 10^{-4}$, no Ledoux term B). The left panels show Kippenhahn diagrams for the primary and the secondary, respectively, together with the total mass evolution of the binary. The panels on the right have the same pattern as figure 1 in Menon et al., 2021. The color scheme is reassigned here: Red background shades indicate strict contact phases ($R/R_{\rm RL} \geq 1$ for both components), gray shades indicate near-contact phases ($0.9 \leq R/R_{\rm RL} < 1$ for both components). Relaxed contact phases are the sum of red and gray phases. The model terminated because of secondary hydrogen depletion.

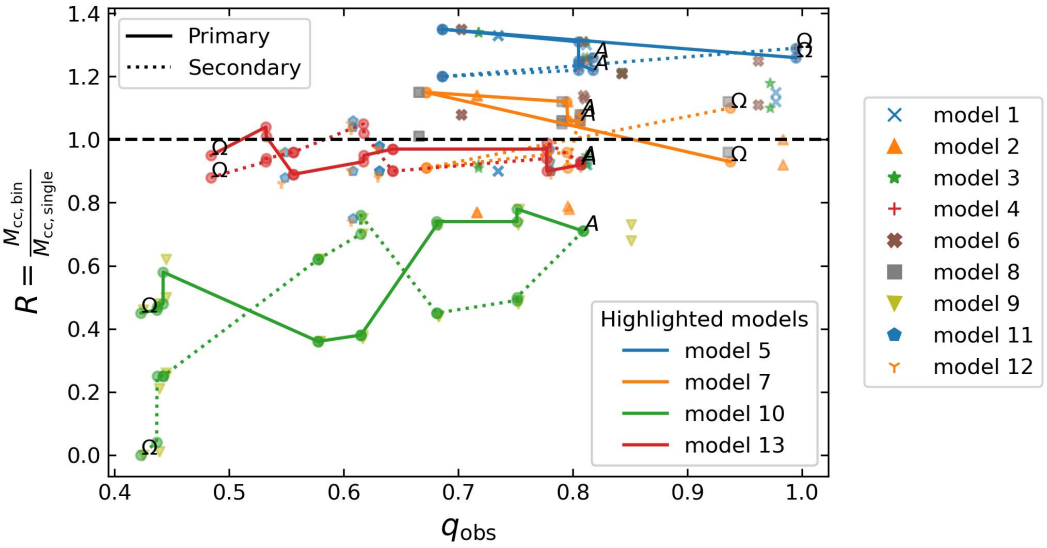

Figure 4.9: Relation between rejuvenation quotient R and observable mass ratio q_{obs} (during relaxed contact). For each model, there is a set of rejuvenation quotients R analogous to the tables in fig. 4.7. Each R is assigned the observable mass ratio q_{obs} the system has at that point in time. The model numbers correspond to table 4.1. Highlighted models indicate typical pathways in this diagram. Points labeled with A indicate the first calculated R at the beginning of the binary evolution, Ω indicates the last one at the end. For not highlighted models, quotients for the primary and the secondary are pooled.

mass transfer on thermal timescale, where mass ratio is inverted. Every model in this thesis has this episode in common. Only models that tend to evolve to minuscule R, and therefore efficiently avoid rejuvenation during episodes of mass transfer (like evolution model 10 in this figure), reach the smallest observable mass ratios. In contrast to that, models evolving to a mass ratio close to $q_{obs} = 1$ (between $0.9 \leq q_{obs} \leq 1.0$, models 5 and 7, for instance) tend to have strongly rejuvenated cores ($R > 0.85$) in the end of their evolution. An avoided rejuvenation (small R) does not occur in this range of q. The points in this interval are slightly separated from the rest. They all have their origin in nuclear timescale contact, where mass ratio tends to be close to one (see section 4.2). Models with more avoided rejuvenation (smaller R) throughout the evolution often evolve preferably to smaller observable mass ratios (cf. highlighted models in fig. 4.9). But still, a strict correlation like $R \propto q_{obs}$ between rejuvenation and the current observable mass ratio cannot be derived from this figure. On the contrary, model 13 is evolving towards small mass ratios *without* any considerable growing delay in rejuvenation.

Figure 4.10 gives the rejuvenation quotients sorted by mean observable mass ratio $\bar{q}_{obs}$ for their corresponding evolution models. As a consequence, it provides a range of rejuvenation occurring during the evolution for every binary evolution model.[4] If rejuvenation was a key phenomenon leading towards $q = 1$ as assumed as hypothesis, this figure would have shown a clear proportionality: The larger R the larger $\bar{q}_{obs}$. This is not the case. On the contrary, model 13 has the most extreme $\bar{q}_{obs}$, even though model 2 (with a $\bar{q}_{obs}$ close to one) occasionally avoids rejuvenation more effectively (the range goes to

[4] Model 13 has a smaller mean observable mass ratio $\bar{q}_{obs}$ than model 10 although model 10 evolves to smaller q_{obs} in fig. 4.9. The reason for this is that model 10 leaves relaxed contact after the third strict contact on thermal timescale (cf. fig. 4.8).

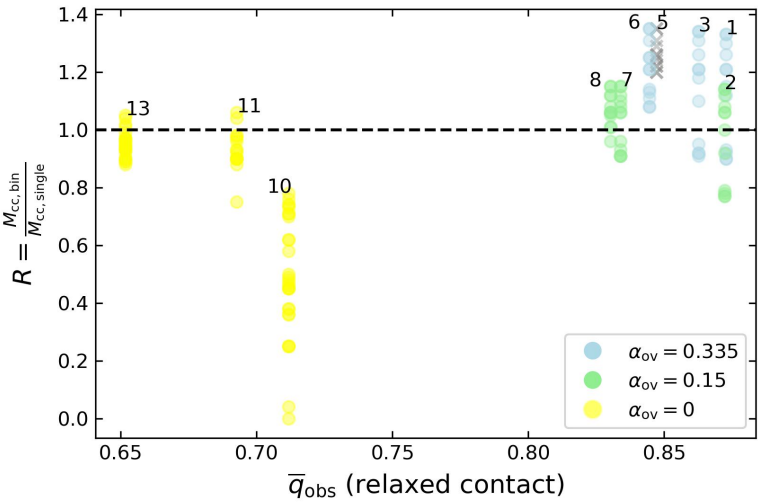

Figure 4.10: Relation between the rejuvenation quotients R (see section 3.6) and mean observable mass ratio $\bar{q}_{obs}$ (see section 3.4) during relaxed contact for the whole evolution model. For each model, there is a set of rejuvenation quotients analogous to the tables in fig. 4.7. The labelled numbers indicate the model numbers corresponding to table 4.1. The colors point out the step overshooting parameter α_{ov} (cf. section 3.1 ff.) following the scheme of fig. 4.11 and table 4.1. Models 4, 9 and 11 are omitted as they are similar to neighboring models (cf. section 4.5).

smaller R than in model 13). But considering the colors indicating the extent of the overshooting region shows that $\bar{q}_{obs}$ is not independent of rejuvenation: Models with a larger overshooting region (marked in blue, for example) tend to rejuvenate more effectively (higher R) and have $\bar{q}_{obs}$ closer to one, whereas models with a smaller overshooting region (marked in yellow, for example) tend to avoid rejuvenation more effectively and have $\bar{q}_{obs}$ far away from one – coinciding with the initial hypothesis. Fixing the extent of the overshooting region, it stands out that rejuvenation has the opposite effect: Models with more rejuvenation (e.g. model 13) have smaller $\bar{q}_{obs}$ than models with an avoided rejuvenation (e.g. model 10). Models with the same color (the same α_{ov}) only differ in their efficiency of semiconvection. Consulting figure 4.11, it turns out that more efficient rejuvenation within a fixed α_{ov} is caused by a higher efficiency of semiconvection. Figure 4.10 therefore shows an overall picture: Rejuvenation driven by a larger extent of the overshooting region leads to $\bar{q}_{obs}$ closer to one, whereas rejuvenation driven by a higher efficiency of semiconvection shifts $\bar{q}_{obs}$ to smaller values.

4.5 Mass Ratio Evolution

This section is intended to give an overview of all calculated binary evolution models, as well as of the impact of the initial parameters on the mean observable mass ratio. Table 4.1 lists all calculated evolution models (one recalculation of System 2 in Menon et al., 2021 and twelve modifications).

Depending on the results in table 4.1, a few models stand out to be similar to their neighbors. Therefore, they stay unregarded in the following sections: First, the combination $\alpha_{ov} = 0.335$ and $B = 10^{-20}$ is very similar to $\alpha_{ov} = 0$ as arising from the pairs of models (11, 12) and (9, 10). Those with $\alpha_{ov} = 0.335$ live slightly longer, but that has no effect on the overall evolution, especially the mean observable mass ratio $\bar{q}_{obs}$ is practically the same. This behavior does not surprise, since $B = 10^{-20}$ strongly constraints the overshooting region as soon as there is a touch of a composition gradient. Moreover, models 5 (system 2 model in Menon et al., 2021) and 4 (same as 5, only with reduced α_{sc}) are absolutely identical. Again, this shows that semiconvection is immaterial in the starting point model 5, as already shown in the Kippenhahn diagrams in fig. 4.1 (section 4.1 shows that overshooting in system 2 straightens the composition gradient where otherwise semiconvection would have occurred).

In consequence of the sorting order, the table is framed by evolution models 1 (with $\bar{q}_{obs}$ closest to one) and 13 (with the smallest $\bar{q}_{obs}$). The evolution of model 1 is depicted in 4.4(a). It stands out due to its fast evolution towards $q_{obs} = 1$ during its contact on nuclear timescale that is typical for type A evolution (for the types, cf. section 4.1). Model 13 is depicted in fig. 4.6(c). It is unique due to its extended total lifetime ($\tau_{tot} = 11.46\,\mathrm{Myr}$), its continuous time spending on relaxed contact ($\tau_{relaxed} = 9.46\,\mathrm{Myr}$) and its consequent avoidance of a strict contact on nuclear timescale that is typical for type C evolution (cf. figures A.1 and A.13).

The strongest effect to the mean observable mass ratio has the evolution type: type A models (models 1 - 6 in table 4.1) generally have a higher $\bar{q}_{obs}$ than type B (models 7 & 8), type B models generally have a higher $\bar{q}_{obs}$ than type C (models 9 - 13). Especially type C models excel in their extreme mass ratios, as models of this type avoid contact on nuclear timescale at all. Consequently, the widest "gap" in $\bar{q}_{obs}$ is between the last type B model 8 (with $\bar{q}_{obs} = 0.830$) and the first type C model (with $\bar{q}_{obs} = 0.713$). Moreover, type C models spend a negligible amount of their total lifespan in an interval $0.95 \leq q_{obs} \leq 1.00$ ($f_{relaxed} \leq 0.01$).

Concerning the effect of the initial parameters on the evolution type, it appears that the type is mainly affected by the extent of the overshooting region: Type C systems practically feature no overshooting at all ($\alpha_{ov} = 0$ or $B = 10^{-20}$), type B systems have a constrained overshooting region ($\alpha_{ov} = 0.15$) and type A usually has an $\alpha_{ov} = 0.335$. Only evolution model 2 falls out of alignment: It features a type A evolution, although its overshooting parameter is $\alpha_{ov} = 0.15$, showing that the extent of the overshooting region driven by the step overshooting parameter α_{ov} cannot be the only key phenomenon determining the type of evolution.

Figure 4.11 illustrates the impact of the mixing parameters to the mean observable mass ratio: Constraining the extent of the overshooting region (reducing α_{ov}) as well as enhancing efficiency of semiconvection (larger α_{sc}) leads to a smaller probability to find a binary system at a mass ratio close to one (smaller $\bar{q}_{obs}$). Additionally, the more overshooting is constrained, the more α_{sc} affects the mean

observable mass ratio (in fig. 4.11, models marked in yellow show a wider range of $\bar{q}_{\mathrm{obs}}$ than models marked in blue). [5]

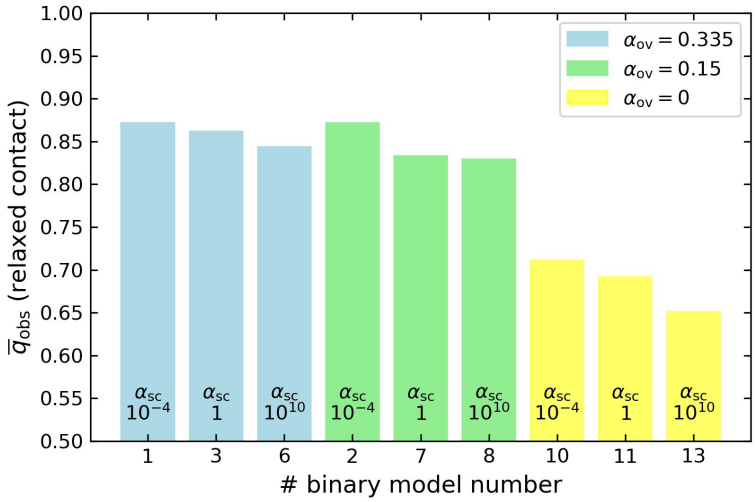

Figure 4.11: Effect of the mixing parameters α_{ov} and α_{sc} (see section 3.1 ff.) on the mean observable mass ratio $\bar{q}_{\mathrm{obs}}$ (see section 3.4) during relaxed contact ($R/R_{\mathrm{RL}} \geq 0.9$ for both components). Binary model numbers correspond to table 4.1. Redundant models are omitted as described in section 4.5.

[5] Model 7 still has a slightly higher mean observable mass ratio than model 8. Concerning the total mass evolution of the components in fig. 4.5(b) and fig. 4.5(c), this may surprise, because the amplitude of the type B mass oscillation during contact on nuclear timescale decreases in model 8 (in other words: the final mass ratio q_{f} of model 8 in table 4.1 is lower than model 7). A closer look at the total mass evolution of both models shows that the contribution of the decreasing amplitude in model 8 to $\bar{q}_{\mathrm{obs}}$ is equalized by the smaller mass transfer rate at the beginning of contact on nuclear timescale.

Table 4.1: Overview of the calculated models, including the step overshooting parameter (α_{ov}), the efficiency parameter of semiconvection (α_{sc}), and the Ledoux term (B) - the threshold in the composition gradient from which the overshooting region is terminated. No value for B means that there is no threshold included in the simulation. The initial mass ratio for every model is $q_i = 0.8$. The table provides the type (see section 4.1), the final mass ratio (q_f) for every simulation, as well as the net simulation lifespan τ_{tot} in Myr. N_{strict} is the amount of strict contact eras. The following values are listed for strict and relaxed contact, repsectively: The duration of contact τ in Myr, q_{min} and q_{max} (the minimum and maximum mass ratio during contact) as well as f (the portion of the contact phase spent at a mass ratio close to one, cf. section 3.5) and $\bar{q}_{obs}$ (the mean observable mass ratio during contact, cf. section 3.4). The table is sorted by $\bar{q}_{obs}$ for relaxed contact (three decimal places for $\bar{q}_{obs}$are needed here to get a clear order). Model 6 (shaded in gray) is a recalculation of "System 2" in Menon et al., 2021. Other colors indicate models with the same combination of α_{ov} and B, redundant models are not colored (cf. text in section 4.5). Bold model numbers were used as examples for representing their types in section 4.1.

	initial parameters						strict contact						relaxed contact				
#	α_{ov}	α_{sc}	B	type	q_f	τ_{tot}	τ	N_{strict}	q_{max}	q_{min}	f	$\bar{q}_{obs}$	τ	q_{max}	q_{min}	f	$\bar{q}_{obs}$
1	0.335	10^{-4}	0.1	A	1.01	9.23	3.88	2	1.36	0.86	0.63	0.937	7.05	1.36	0.81	0.34	0.873
2	0.15	10^{-4}	0.1	A	1.01	8.72	3.52	2	1.40	0.85	0.75	0.951	6.66	1.40	0.81	0.40	0.872
3	0.335	1	0.1	A	1.02	9.32	3.63	2	1.39	0.86	0.63	0.935	7.14	1.39	0.81	0.32	0.863
4	0.335	10^{-4}	-	A	1.00	9.81	3.37	2	1.46	0.85	0.66	0.941	7.63	1.46	0.81	0.29	0.847
5	0.335	1	-	A	1.00	9.81	3.37	2	1.46	0.85	0.66	0.941	7.63	1.46	0.81	0.29	0.847
6	0.335	10^{10}	0.1	A	1.03	9.50	3.46	2	1.42	0.86	0.39	0.916	7.32	1.42	0.81	0.19	0.845
7	0.15	1	0.1	B	1.05	9.06	2.88	2	1.49	0.85	0.51	0.934	7.00	1.49	0.81	0.21	0.834
8	0.15	10^{10}	0.1	B	1.03	9.14	2.81	2	1.50	0.85	0.54	0.937	7.08	1.50	0.81	0.21	0.830
9	0.335	10^{-4}	10^{-20}	C	2.35	8.79	0.48	4	2.35	0.58	0.06	0.734	5.03	2.35	0.58	0.01	0.713
10	0	10^{-4}	-	C	2.36	8.78	0.45	4	2.36	0.58	0.04	0.733	5.04	2.36	0.58	0.00	0.712
11	0	1	-	C	0.89	9.21	0.47	3	1.58	0.55	0.04	0.683	7.31	1.58	0.55	0.00	0.693
12	0.335	1	10^{-20}	C	0.83	9.30	0.46	3	1.59	0.55	0.04	0.679	7.39	1.59	0.55	0.00	0.691
13	0	10^{10}	-	C	1.68	11.46	0.69	4	2.07	0.56	0.03	0.657	9.46	2.07	0.56	0.00	0.652

CHAPTER 5

Discussion

It is worth to consider the mixing parameters investigated in this thesis (cf. sec. 3.3) as arbitrary choices. Although α_{sc} was estimated to be a factor of order unity in Langer, Fricke and Sugimoto, 1983 and α_{ov} was calibrated to $\alpha_{\mathrm{ov}} = 0.335$ in Brott et al., 2011 (coinciding with the mass range for the models in this thesis), the selection of initial parameters that reflects physical reality is not reliably known (Pols, 2009). Hence, choosing extreme cases for the mixing parameters were only intended to show the effect of rejuvenation on the mean observable mass ratio, without claiming physical truth. The Ledoux term, commonly set to $B = 0.1$, even was an arbitrary choice in Marchant, 2018 (chapter 5), as the stabilizing effect to overshooting of the gradient in mean molecular weight is not certain. Marchant, 2018 showed for $B = 0.2$ and $B = 0.05$ that the choice of this parameter had no significant impact on their models. In contrast, models 9 and 12 in this thesis (cf. table 4.1) show that a very strict value for B can effectively constrain the overshooting region, change the type of evolution and significantly alter the mean observable mass ratio $\bar{q}_{\mathrm{obs}}$.[1]

Also, the methods used for the evaluation of certainly succumb to uncertainties. In the calculation of the rejuvenation quotient R (as described in section 3.6) $M_{\mathrm{cc,single}}$ does not account for the overshooting region, as its extent is not provided by the source of data in fig. 3.2. Consequently, all values of R in figures 4.9 and 4.10 are expected to be shifted to lower R, as the divisor $M_{\mathrm{cc,single}}$ is missing a constant summand[2]. That is not expected to change the results too much, as every value for R is affected almost equally. Furthermore, $\bar{q}_{\mathrm{obs}}$and f used in table 4.1 give an orientation, but not the concrete probability distribution of observed mass ratios as given in Menon et al., 2021, fig. 9.[3] For this purpose, a grid of models would have to be created for each combination of α_{sc}, α_{ov} and B.

Comparing the results to the grid in Menon et al., 2021, many common features stand out: They point out that their binary evolution models being in contact over nuclear timescale inevitably merge. That also applies for models in this thesis: All type A and B models featuring a contact on nuclear timescale are terminated due to L_2 overflow and are consequently expected to merge (see termination reasons in the captions of the appendix chapter A). The only two models that are terminated because of

[1] Still, $B = 10^{-20}$ is arbitrarily chosen and extremely strict. That the value for B meeting with nature is still this small, can be doubted, as it leads to practically suppressing overshooting at all in the models of this thesis. Nevertheless, how strong a gradient in molecular weight keeps off overshooting from mixing through the stellar envelope, is still uncertain.

[2] The extent of the overshooting region in the models that deliver the correlation in fig. 3.2 is assumed to be approximately constant, because step overshooting ($\alpha_{\mathrm{ov}} = 0.335$) was accounted. $B = 0.1$ (also implemented in these models) is not expected to constrain the overshooting region, because models in this thesis do not show a relevant effect of $B = 0.1$, as long as there is no mass transferred (for example, see Kippenhahn diagrams in fig. 4.4 during the initial detached phase).

[3] That can be specifically seen by comparing $f_{\mathrm{relaxed}} = 0.29$ for model 5 in table 4.1 with $H_{\mathrm{contact}}\,(0.95 \leq q \leq 1) = 0.5$ in Menon et al., 2021, fig. 9. They are not equal.

secondary hydrogen depletion (they survive the main sequence) are of type C (see fig. A.9 and A.10)– consequently, they avoid contact on nuclear timescale. Furthermore, nuclear timescale contact binaries evolve nearly towards equal masses – coinciding with Menon et al., 2021. The only difference is that with a constrained overshooting, there is a mass ratio oscillation around unity, leading to a higher probability to observe them at mass ratios further away from 1. Moreover, they point out that "the longer a system spends time in contact, the likelier it attains a mass ratio of 1". Models in this thesis show that mass ratio oscillations during contact may prevent a constant evolution to an equal mass binary (cf. model 7 in figure 4.5(b)). On the other hand, model 8 (fig. 4.5(c)) shows that type B evolution can also feature a decreasing amplitude of mass ratio oscillation. This may also be described as a constant evolution towards an equal-mass binary. Finally, they also conclude that "observed unequal-mass contact systems are likely to be binaries just nearing contact". This is also valid for the models of this thesis: All systems have the smallest observable mass ratios during near-contact phases. At phases of strict contact, they tend to spend more time at mass ratios closer to one (cf. gray and red shaded phases in fig. 4.3).

The type B mass ratio oscillation (as described in section 4.1) is not a totally new phenomenon in stellar evolution models: Models in this thesis do not account for energy transfer as described in the introduction chapter 1. Type B mass ratio oscillation also occurs in binary evolution models, accounting for energy transfer in Fabry et al., 2023. It is imaginable that a combination of a constrained overshooting region, that mainly leads to type B evolution in this thesis, with their methodology to account for energy transfer could amplify the mass ratio oscillation. A bigger amplitude of the q oscillation would lead to less time spent at q_{obs} close to one. Mass ratio oscillation during strict contact also occurs at models accounting for chemically homogeneous evolution in Marchant et al., 2016. These models do not follow type B evolution, as they avoid contact on thermal timescale. Anyway, this channel of mass ratio oscillation is not relevant for the models in this thesis, as the total mass range considers substantial higher masses ($M_{\mathrm{component}} \gtrsim 20\,\mathrm{M}_{\odot}$).

Considering the observations in fig. 9 of Menon et al., 2021, one can estimate, if one of the calculated models in this thesis could meet the requirement of a reduced probability to find a system at a mass ratio close to one: Model 5 in tab. 4.1 with $f_{\mathrm{relaxed}} = 0.29$ does not meet the observations as emerged from Menon et al., 2021. Type B evolution reduces f only slightly (on strict as well as on relaxed contact). Hence, most of the observations would be still expected at a mass ratio close to one. Consequently, the amplitude of the mass ratio oscillation is not expected to be sufficient to explain the observations. Accounting for energy transfer as described could alleviate that the amplitude is too small. In contrast, type C models spend a *negligible* amount of their total lifespan in an interval $0.95 \leq q_{\mathrm{obs}} \leq 1.00$ ($f_{\mathrm{relaxed}} \leq 0.01$ in table 4.1). Considering the observed contact systems that are summarized in Menon et al., 2021, fig. 9, at least 5 of them are in this interval. It was extremely improbable to observe binaries within this interval, if they would follow a type C evolution.

Hence, it is doubtful that the initial parameters that lead to a type C evolution totally comply with nature. On the other hand, initial parameters leading to a type C evolution are only calculated for one starting point model, without considering a whole grid. It is imaginable that binary configurations with smaller orbital periods may lead to a contact phase on nuclear timescale despite having initial type C parameters. An additional contact on nuclear timescale leading to a considerable amount of time the system spends at a mass ratio close to one – next to an extensive lifetime during a semi-detached configuration as typical for type C – would not exclude an observation of q_{obs} close to one and could still explain the higher probability to find a binary system at mass ratio further away from one. An initial

$q_{\mathrm{i}} \approx 1$ with a small initial orbital period (so that the system already starts being in near-contact) could operate analogously.

In summary: While models following type B evolution reduce f too less, models with type C evolution do too much. Nevertheless, this thesis is not intended to give a concrete calibration of the mixing parameters.

CHAPTER 6

Conclusion

In this thesis, an examination of the effect of rejuvenation to the mass ratio evolution in massive contact binaries was performed. The nature of this work is intended as follow-up study of Menon et al., 2021, where the population of binaries found at a mass ratio close to one was over-estimated. 12 detailed binary evolution models (and one recalculation) were computed in MESA, in which rejuvenation occurs with varying efficiency, by modifying physics of overshooting and semiconvection.

The evolution models showed that modifying the mixing parameters can significantly change the mass ratio evolution. The models are divided in three evolution types, depending on their appearance in mass ratio evolution: Type A models do not change their overall evolution and stick to the models in Menon et al., 2021 instead. Type B models rather undergo a mass ratio oscillation around unity than approaching to equal masses during contact. Type C models avoid a contact configuration on a long, nuclear timescale at all (cf. section 4.1).

By comparison of all models, it stands out that the evolution type is mainly affected by the extent of the overshooting region: A reduced extent ($\alpha_{\rm ov} = 0.15$) usually leads to a type B evolution. Turning off overshooting ($\alpha_{\rm ov} = 0$) leads to a type C evolution, effectively avoiding the contact on nuclear timescale. In contrast, semiconvection usually does not affect the overall evolution type. Instead, a higher efficiency of semiconvection leads preferably to an enlarged lifespan of the semi-detached phases, where the observable mass ratio monotonically decreases. Strictly constraining the extent of overshooting concedes semiconvection to carry more weight by reducing the mean observable mass ratio, as evolution is dominated by semi-detached configurations (cf. section 4.5).

Rejuvenation is driven by the mixing parameters: A higher efficiency of semiconvection as well as an enlarge extent of the overshooting region leads to more efficient rejuvenation. The binary evolution model from Menon et al., 2021 that was used as a starting point features instantaneous rejuvenation. Comparing the different degrees of rejuvenation in this thesis, a general statement as assumed as hypothesis in the introductory chapter 1 like "more avoided rejuvenation throughout the whole evolution leads to smaller observable mass ratio" turns out to be incorrect. Instead, another overall picture arises: Rejuvenation driven by a larger extent of the overshooting region (higher $\alpha_{\rm ov}$) leads to a mean observable mass ratio $\bar{q}_{\rm obs}$ closer to one. But rejuvenation driven by a higher efficiency of semiconvection (higher $\alpha_{\rm sc}$) leads to a *reduced* $\bar{q}_{\rm obs}$, further away from unity, as it preferably affects the semi-detached configurations. Still, this thesis shows that rejuvenation is closely linked to the overall mass ratio evolution. In particular, a binary that is at a mass ratio close to one *currently*, has highly rejuvenated cores (cf. fig. 4.9 & section 4.4).

Considering the overall outcomes of the models in this thesis, two new directions for prospective

studies emerge:

Further studies could investigate in the mass ratio oscillation during contact, as it occurs in type B evolution. The mass ratio amplitude for the models in this thesis is not sufficient (as described in the discursive chapter 5). It is conceivable that a combination of reduced rejuvenation (via a constrained overshooting region) in this thesis with accounting for energy transfer analogously to Fabry et al., 2023 could sufficiently increase the amplitude of the mass ratio oscillation.

Moreover, as type C evolution stands out with its considerable small mean observable mass ratio (cf. fig. 4.11), this kind of evolution may indicate the most auspicious channel that could explain the discrepancy of the overestimated population of binaries at a mass ratio close to one. It may be worth to investigate in the exact cause that determines whether stars stay in contact on nuclear timescale or break it off by detaching, because preventing a contact on nuclear timescale seems to affect the mean observable mass ratio most. A detailed knowledge of the circumstances that cause a detaching could furthermore support an explanation, why a negligible extent of the overshooting region causes the prevention of contact at nuclear timescale. Nevertheless, type C models in this thesis can be doubted to reflect nature (as described in the discursive chapter 5). To show their reasonability is up to a new detailed grid of binary evolution models, analogously to[1] Menon et al., 2021.

[1] Has it happened often enough for this work to be cited? Let us quote their paper one last time...

APPENDIX A

Calculated models in detail

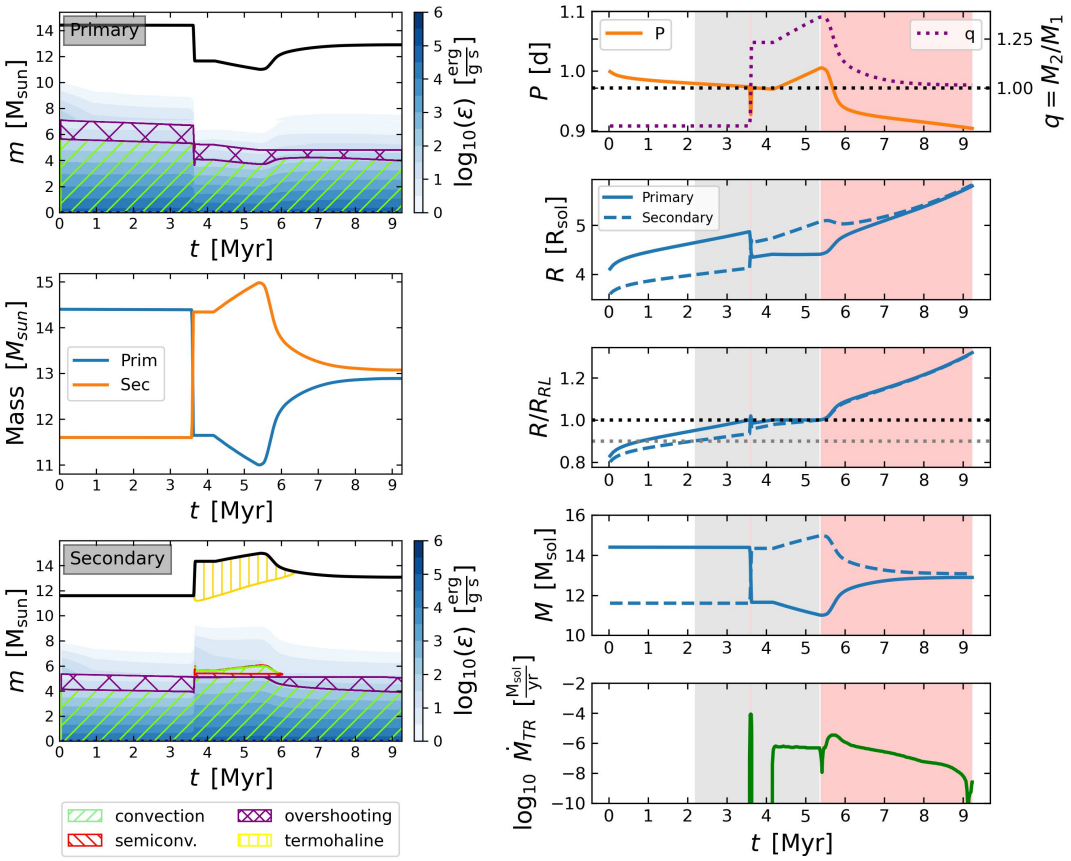

Figure A.1: Model number 1 in table 4.1 with the mixing parameters $\alpha_{\rm ov} = 0.335$, $\alpha_{\rm sc} = 10^{-4}$, $B = 0.1$. Initial masses $M_{1,\rm i} = 14.4$, and $M_{2,\rm i} = 11.6$, and initial orbital period $P_{\rm i} = 1$ d are the same for all models. The left panels show Kippenhahn diagrams for the primary and the secondary, respectively, together with the total mass evolution of the binary. The panels on the right have the same pattern as figure 1 in Menon et al., 2021. The color scheme is reassigned here: Red background shades indicate strict contact phases ($R/R_{\rm RL} \geq 1$ for both components), gray shades indicate near-contact phases ($0.9 \leq R/R_{\rm RL} < 1$ for both components). The model terminated because of L2 overflow.

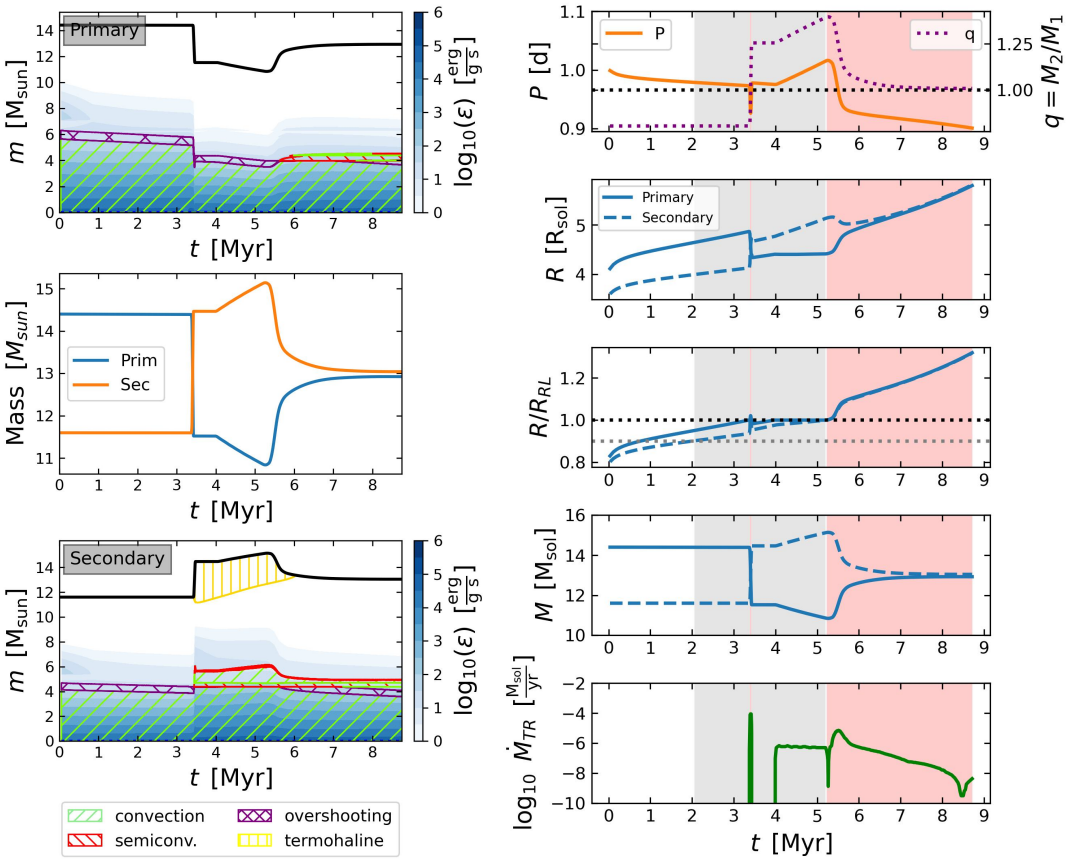

Figure A.2: Model number 2 in table 4.1 with the mixing parameters $\alpha_{\rm ov} = 0.15, \alpha_{\rm sc} = 10^{-4}, B = 0.1$. Initial masses $M_{1,\rm i} = 14.4$, and $M_{2,\rm i} = 11.6$, and initial orbital period $P_{\rm i} = 1$ d are the same for all models. The left panels show Kippenhahn diagrams for the primary and the secondary, respectively, together with the total mass evolution of the binary. The panels on the right have the same pattern as figure 1 in Menon et al., 2021. The color scheme is reassigned here: Red background shades indicate strict contact phases ($R/R_{\rm RL} \geq 1$ for both components), gray shades indicate near-contact phases ($0.9 \leq R/R_{\rm RL} < 1$ for both components). The model terminated because of L2 overflow.

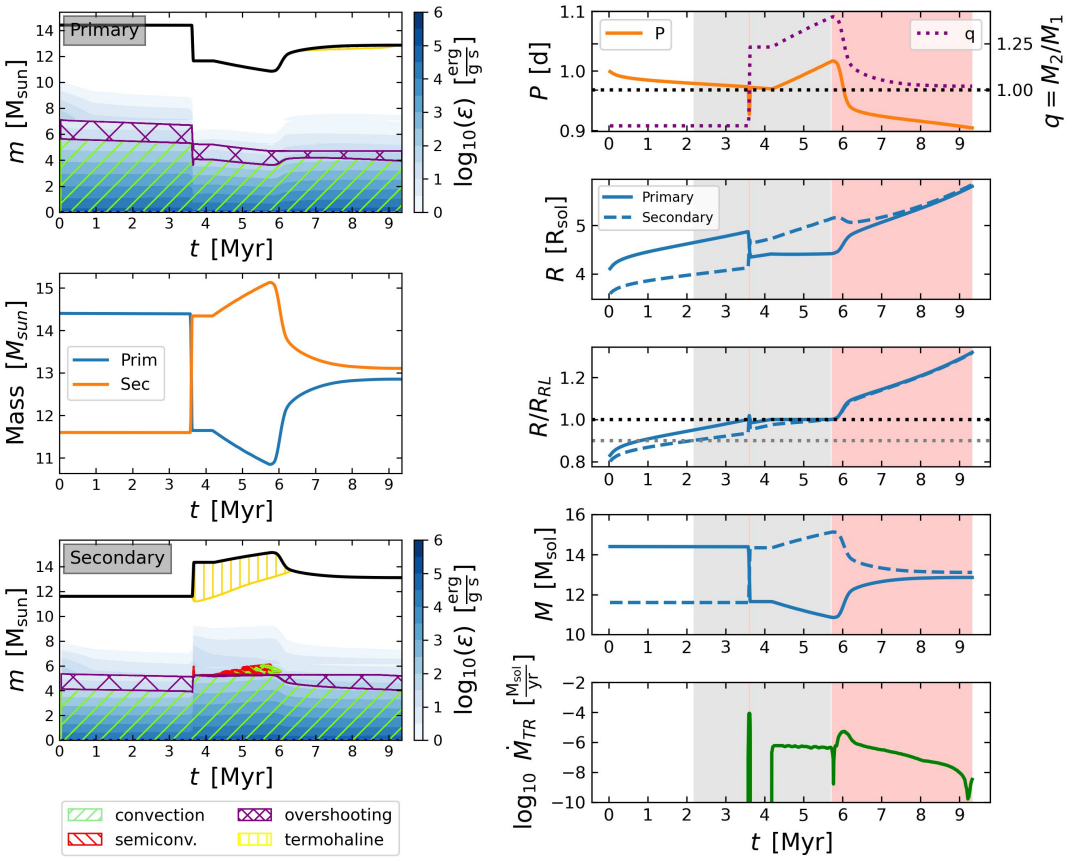

Figure A.3: Model number 3 in table 4.1 with the mixing parameters $\alpha_{\rm ov} = 0.335, \alpha_{\rm sc} = 1.0, B = 0.1$. Initial masses $M_{1,\rm i} = 14.4$, and $M_{2,\rm i} = 11.6$, and initial orbital period $P_{\rm i} = 1$ d are the same for all models. The left panels show Kippenhahn diagrams for the primary and the secondary, respectively, together with the total mass evolution of the binary. The panels on the right have the same pattern as figure 1 in Menon et al., 2021. The color scheme is reassigned here: Red background shades indicate strict contact phases ($R/R_{\rm RL} \geq 1$ for both components), gray shades indicate near-contact phases ($0.9 \leq R/R_{\rm RL} < 1$ for both components). The model terminated because of L2 overflow.

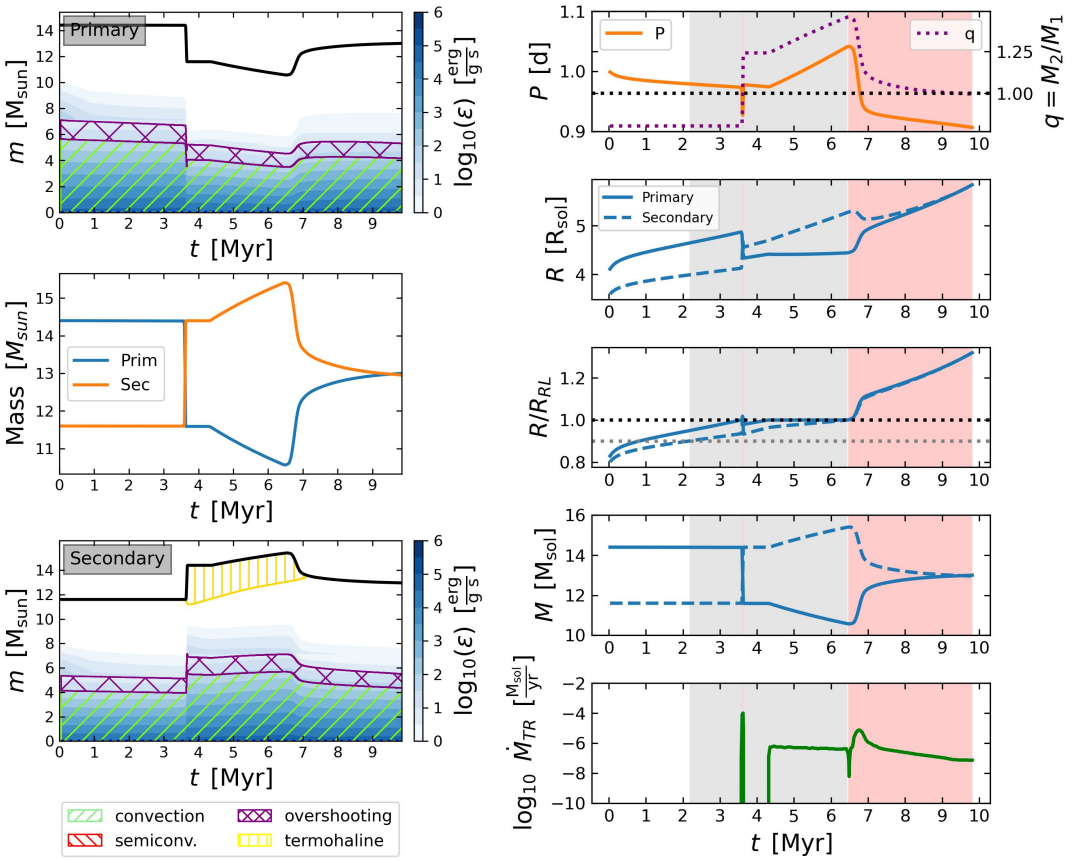

Figure A.4: Model number 4 in table 4.1 with the mixing parameters $\alpha_{\rm ov} = 0.335, \alpha_{\rm sc} = 10^{-4}, B = -$. Initial masses $M_{1,\rm i} = 14.4$, and $M_{2,\rm i} = 11.6$, and initial orbital period $P_{\rm i} = 1$ d are the same for all models. The left panels show Kippenhahn diagrams for the primary and the secondary, respectively, together with the total mass evolution of the binary. The panels on the right have the same pattern as figure 1 in Menon et al., 2021. The color scheme is reassigned here: Red background shades indicate strict contact phases ($R/R_{\rm RL} \geq 1$ for both components), gray shades indicate near-contact phases ($0.9 \leq R/R_{\rm RL} < 1$ for both components). The model terminated because of L2 overflow.

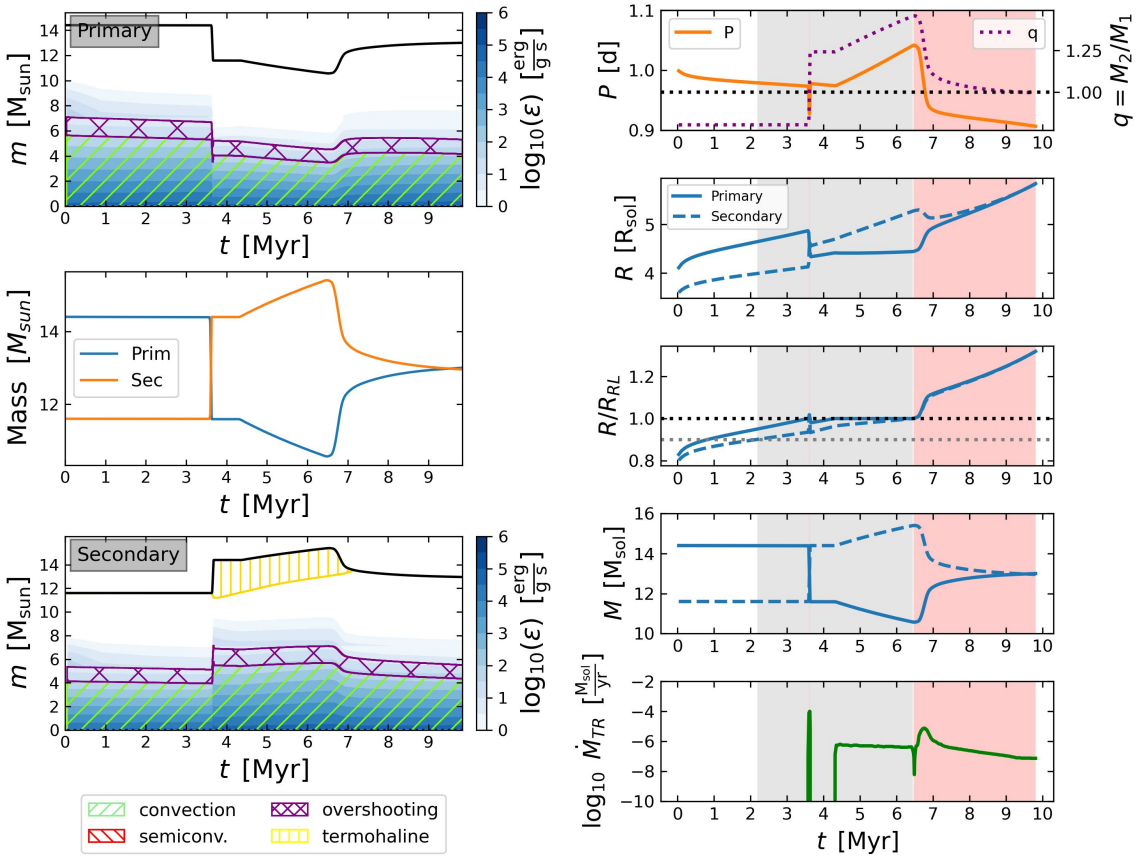

Figure A.5: Model number 5 in table 4.1 with the mixing parameters $\alpha_{\rm ov} = 0.335$, $\alpha_{\rm sc} = 1.0$, $B = -$. Initial masses $M_{1,\rm i} = 14.4$, and $M_{2,\rm i} = 11.6$, and initial orbital period $P_{\rm i} = 1$ d are the same for all models. The left panels show Kippenhahn diagrams for the primary and the secondary, respectively, together with the total mass evolution of the binary. The panels on the right have the same pattern as figure 1 in Menon et al., 2021. The color scheme is reassigned here: Red background shades indicate strict contact phases ($R/R_{\rm RL} \geq 1$ for both components), gray shades indicate near-contact phases ($0.9 \leq R/R_{\rm RL} < 1$ for both components). The model terminated because of L2 overflow.

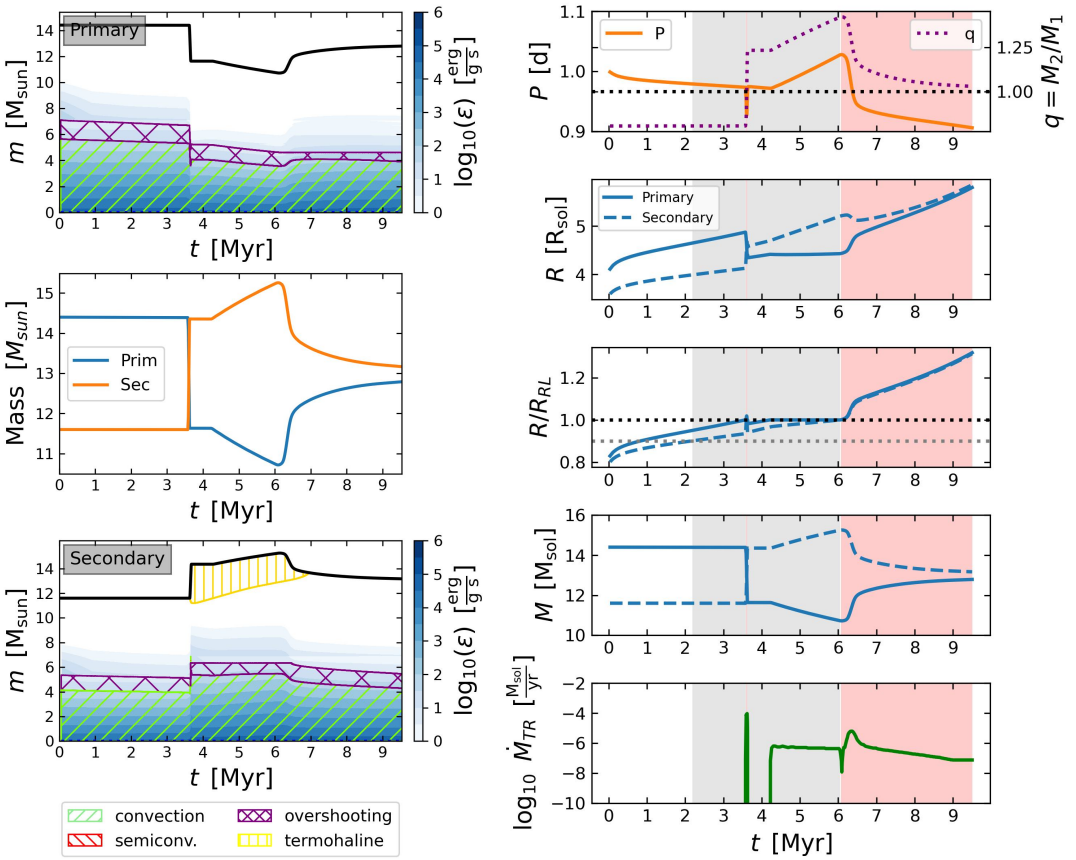

Figure A.6: Model number 6 in table 4.1 with the mixing parameters $\alpha_{\rm ov} = 0.335, \alpha_{\rm sc} = 10^{10}, B = 0.1$. Initial masses $M_{1,\rm i} = 14.4$, and $M_{2,\rm i} = 11.6$, and initial orbital period $P_{\rm i} = 1$ d are the same for all models. The left panels show Kippenhahn diagrams for the primary and the secondary, respectively, together with the total mass evolution of the binary. The panels on the right have the same pattern as figure 1 in Menon et al., 2021. The color scheme is reassigned here: Red background shades indicate strict contact phases ($R/R_{\rm RL} \geq 1$ for both components), gray shades indicate near-contact phases ($0.9 \leq R/R_{\rm RL} < 1$ for both components). The model terminated because of L2 overflow.

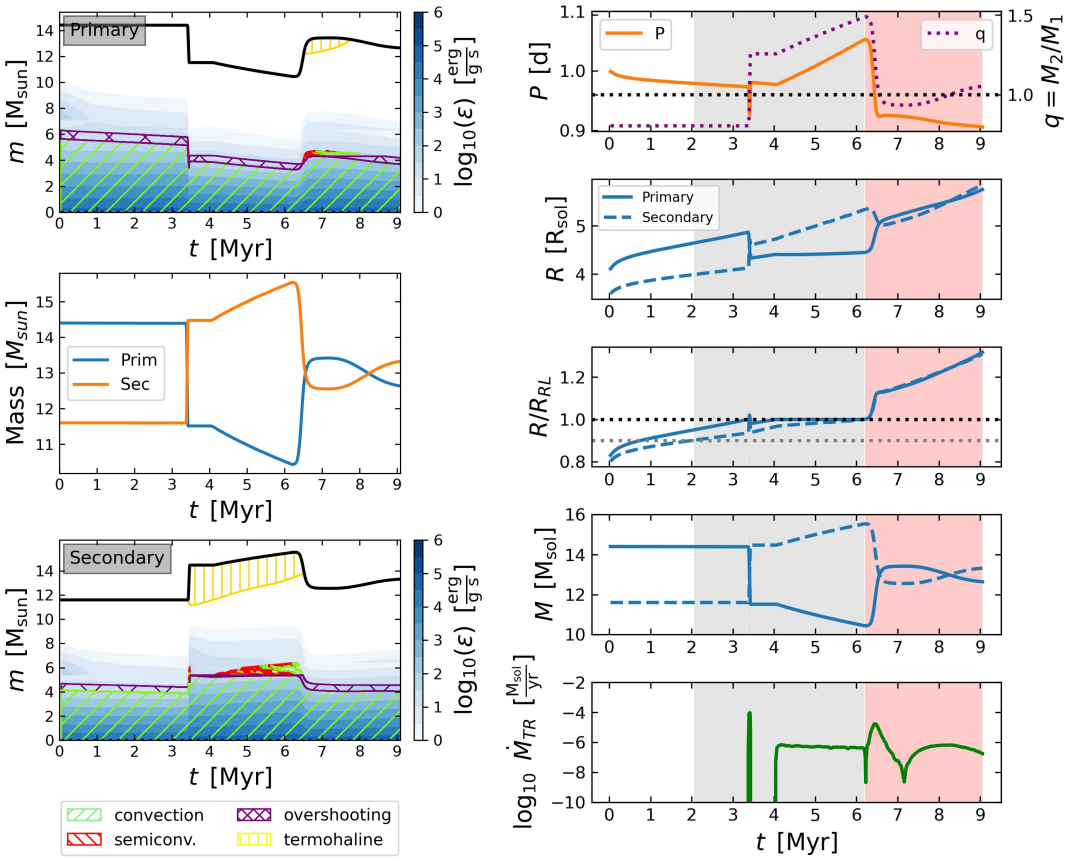

Figure A.7: Model number 7 in table 4.1 with the mixing parameters $\alpha_{\rm ov} = 0.15$, $\alpha_{\rm sc} = 1.0$, $B = 0.1$. Initial masses $M_{1,\rm i} = 14.4$, and $M_{2,\rm i} = 11.6$, and initial orbital period $P_{\rm i} = 1$ d are the same for all models. The left panels show Kippenhahn diagrams for the primary and the secondary, respectively, together with the total mass evolution of the binary. The panels on the right have the same pattern as figure 1 in Menon et al., 2021. The color scheme is reassigned here: Red background shades indicate strict contact phases ($R/R_{\rm RL} \geq 1$ for both components), gray shades indicate near-contact phases ($0.9 \leq R/R_{\rm RL} < 1$ for both components). The model terminated because of L2 overflow.

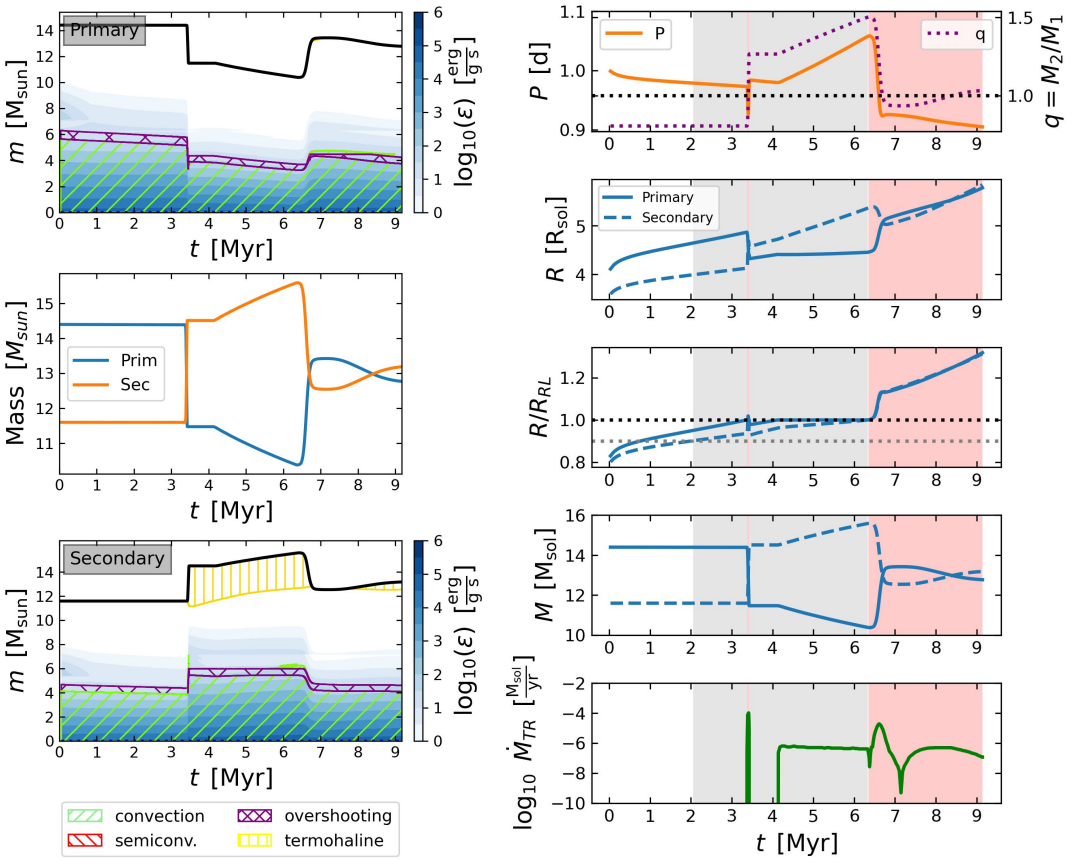

Figure A.8: Model number 8 in table 4.1 with the mixing parameters $\alpha_{\rm ov} = 0.15, \alpha_{\rm sc} = 10^{10}, B = 0.1$. Initial masses $M_{1,\rm i} = 14.4$, and $M_{2,\rm i} = 11.6$, and initial orbital period $P_{\rm i} = 1$ d are the same for all models. The left panels show Kippenhahn diagrams for the primary and the secondary, respectively, together with the total mass evolution of the binary. The panels on the right have the same pattern as figure 1 in Menon et al., 2021. The color scheme is reassigned here: Red background shades indicate strict contact phases ($R/R_{\rm RL} \geq 1$ for both components), gray shades indicate near-contact phases ($0.9 \leq R/R_{\rm RL} < 1$ for both components). The model terminated because of L2 overflow.

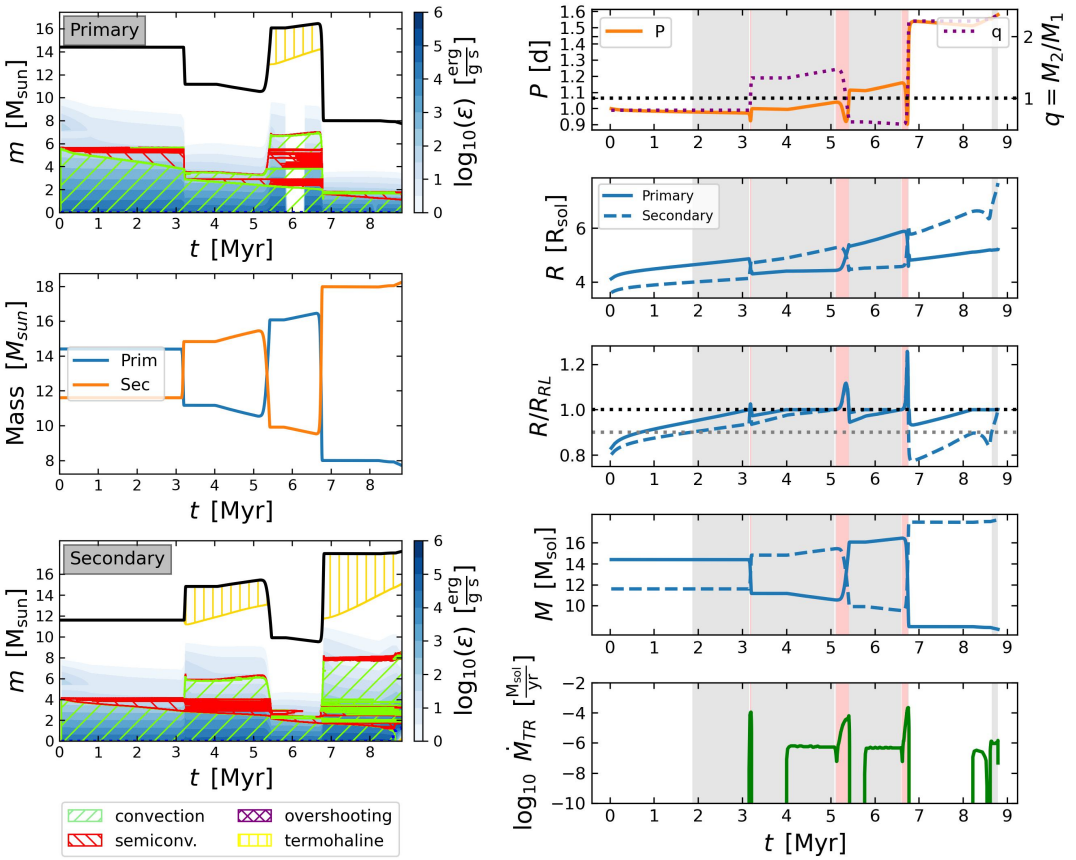

Figure A.9: Model number 9 in table 4.1 with the mixing parameters $\alpha_{\rm ov} = 0.335$, $\alpha_{\rm sc} = 10^{-4}$, $B = 1e-20$. Initial masses $M_{1,\rm i} = 14.4$, and $M_{2,\rm i} = 11.6$, and initial orbital period $P_{\rm i} = 1$ d are the same for all models. The left panels show Kippenhahn diagrams for the primary and the secondary, respectively, together with the total mass evolution of the binary. The panels on the right have the same pattern as figure 1 in Menon et al., 2021. The color scheme is reassigned here: Red background shades indicate strict contact phases ($R/R_{\rm RL} \geq 1$ for both components), gray shades indicate near-contact phases ($0.9 \leq R/R_{\rm RL} < 1$ for both components). The model terminated because of central hydrogen depletion.

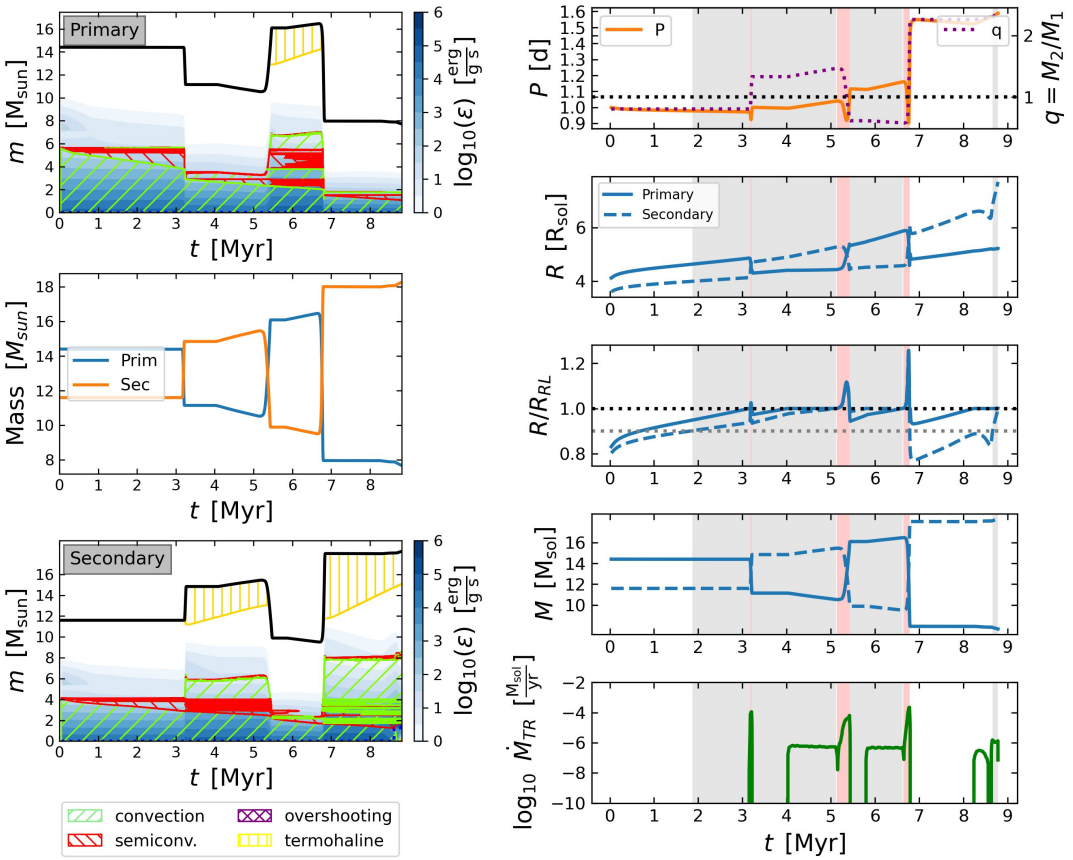

Figure A.10: Model number 10 in table 4.1 with the mixing parameters $\alpha_{\rm ov} = 0, \alpha_{\rm sc} = 10^{-4}, B = -$. Initial masses $M_{1,\rm i} = 14.4$, and $M_{2,\rm i} = 11.6$, and initial orbital period $P_{\rm i} = 1$ d are the same for all models. The left panels show Kippenhahn diagrams for the primary and the secondary, respectively, together with the total mass evolution of the binary. The panels on the right have the same pattern as figure 1 in Menon et al., 2021. The color scheme is reassigned here: Red background shades indicate strict contact phases ($R/R_{\rm RL} \geq 1$ for both components), gray shades indicate near-contact phases ($0.9 \leq R/R_{\rm RL} < 1$ for both components). The model terminated because of secondary hydrogen depletion.

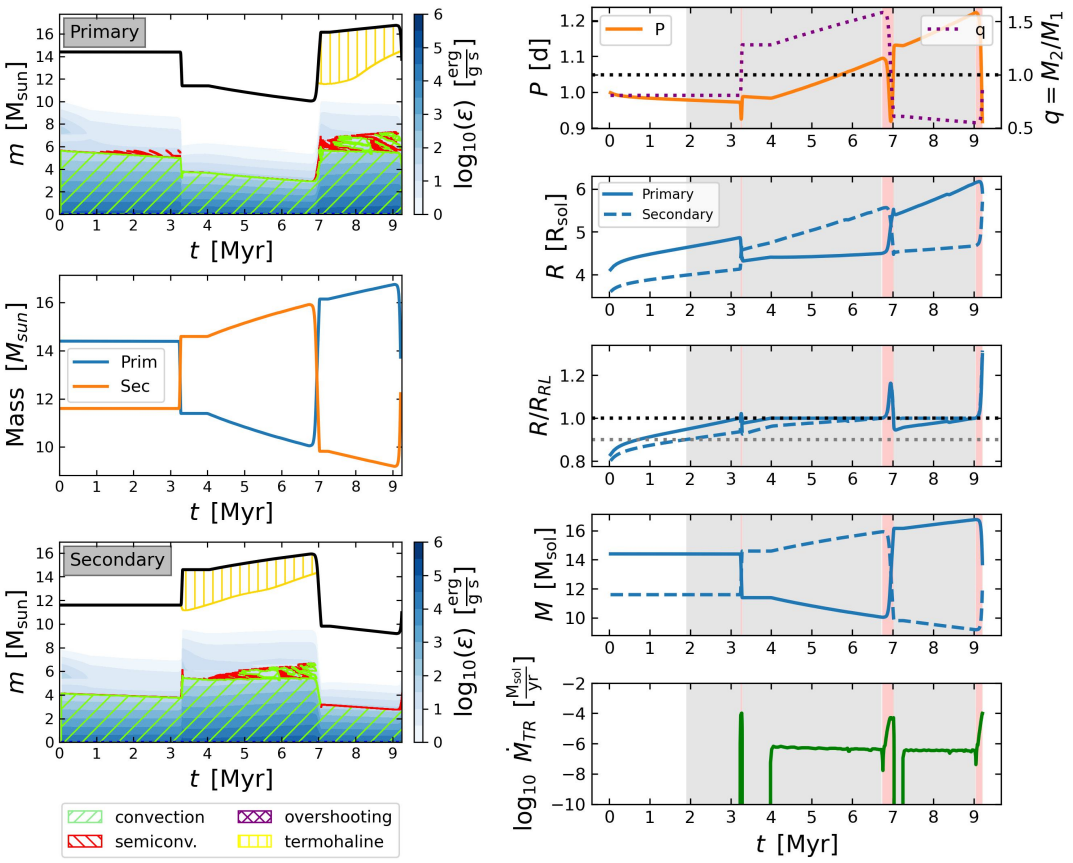

Figure A.11: Model number 11 in table 4.1 with the mixing parameters $\alpha_{\rm ov} = 0, \alpha_{\rm sc} = 1.0, B = -$. Initial masses $M_{1,\rm i} = 14.4$, and $M_{2,\rm i} = 11.6$, and initial orbital period $P_{\rm i} = 1$ d are the same for all models. The left panels show Kippenhahn diagrams for the primary and the secondary, respectively, together with the total mass evolution of the binary. The panels on the right have the same pattern as figure 1 in Menon et al., 2021. The color scheme is reassigned here: Red background shades indicate strict contact phases ($R/R_{\rm RL} \geq 1$ for both components), gray shades indicate near-contact phases ($0.9 \leq R/R_{\rm RL} < 1$ for both components). The model terminated because of L2 overflow.

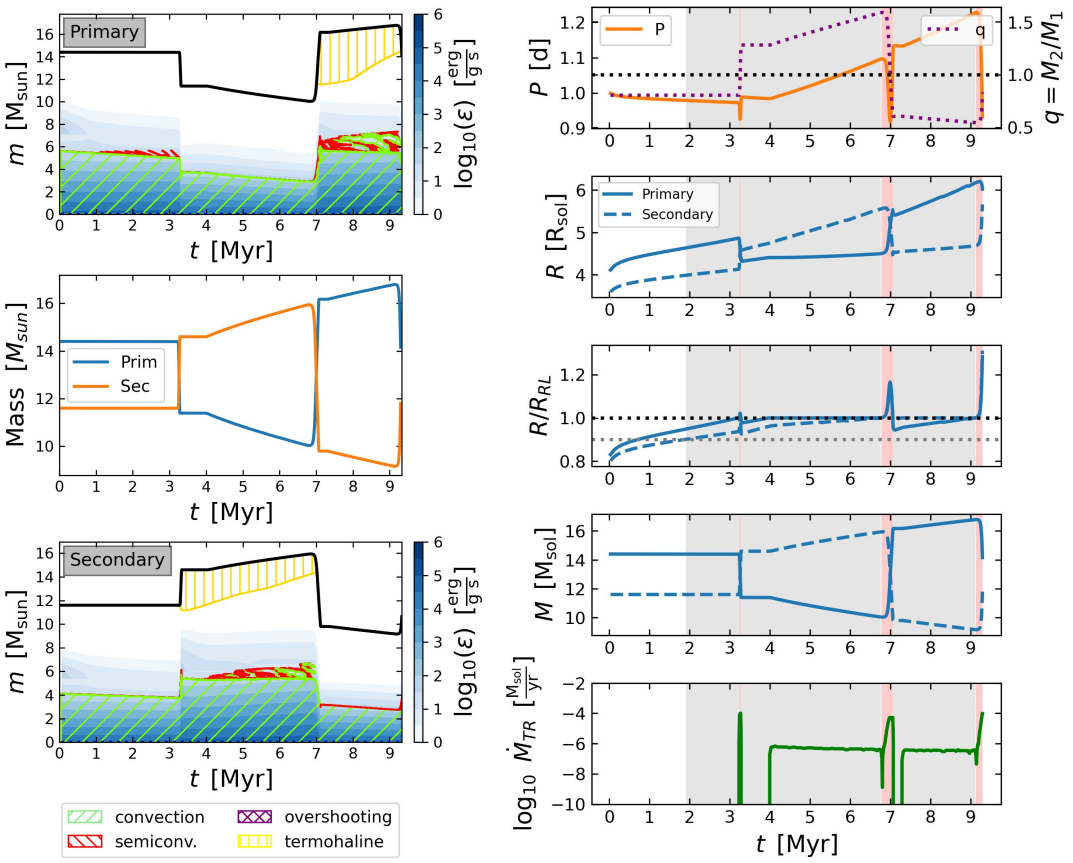

Figure A.12: Model number 12 in table 4.1 with the mixing parameters $\alpha_{\rm ov} = 0.335, \alpha_{\rm sc} = 1.0, B = 1e-20$. Initial masses $M_{1,\rm i} = 14.4$, and $M_{2,\rm i} = 11.6$, and initial orbital period $P_{\rm i} = 1$ d are the same for all models. The left panels show Kippenhahn diagrams for the primary and the secondary, respectively, together with the total mass evolution of the binary. The panels on the right have the same pattern as figure 1 in Menon et al., 2021. The color scheme is reassigned here: Red background shades indicate strict contact phases ($R/R_{\rm RL} \geq 1$ for both components), gray shades indicate near-contact phases ($0.9 \leq R/R_{\rm RL} < 1$ for both components). The model terminated because of L2 overflow.

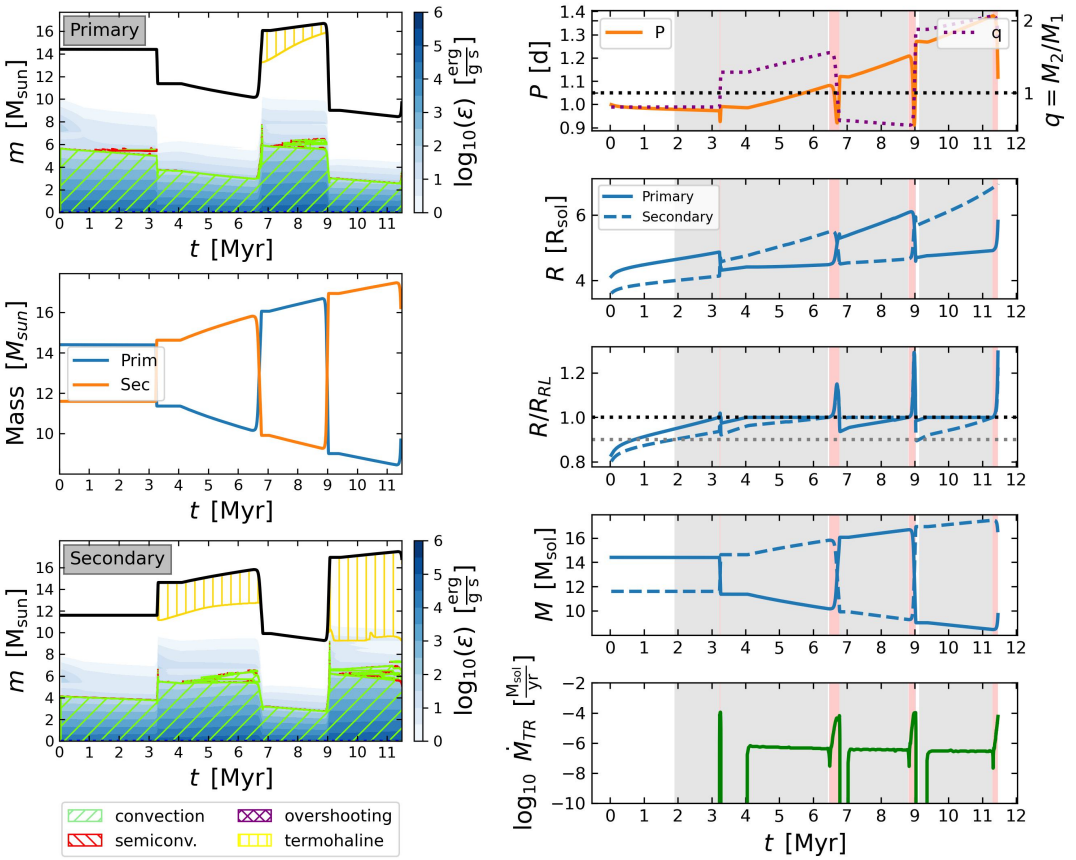

Figure A.13: Model number 13 in table 4.1 with the mixing parameters $\alpha_{\rm ov} = 0, \alpha_{\rm sc} = 10^{10}, B = -$. Initial masses $M_{1,\rm i} = 14.4$, and $M_{2,\rm i} = 11.6$, and initial orbital period $P_{\rm i} = 1$ d are the same for all models. The left panels show Kippenhahn diagrams for the primary and the secondary, respectively, together with the total mass evolution of the binary. The panels on the right have the same pattern as figure 1 in Menon et al., 2021. The color scheme is reassigned here: Red background shades indicate strict contact phases ($R/R_{\rm RL} \geq 1$ for both components), gray shades indicate near-contact phases ($0.9 \leq R/R_{\rm RL} < 1$ for both components). The model terminated because of L2 overflow.

Bibliography

Boer, K. de (2008), *Stars and Stellar Evolution*, eng, France: EDP Sciences, ISBN: 2759803287 (cit. on pp. 7, 9, 11).

Braun, H. and N. Langer (1995), *Effects of accretion onto massive main sequence stars.*, **297** 483 (cit. on p. 3).

Brott, I. et al. (2011), *Rotating massive main-sequence stars. I. Grids of evolutionary models and isochrones*, **530**, A115 A115, arXiv: 1102.0530 [astro-ph.SR] (cit. on pp. 13, 37).

de Mink, S. E., N. Langer, R. G. Izzard, H. Sana and A. de Koter (2013), *The Rotation Rates of Massive Stars: The Role of Binary Interaction through Tides, Mass Transfer, and Mergers*, **764**, 166 166, arXiv: 1211.3742 [astro-ph.SR] (cit. on p. 1).

Eggleton, P. P. (1983), *Aproximations to the radii of Roche lobes.*, **268** 368 (cit. on p. 1).

ESO/L. Calçada (2023), URL: http://www.eso.org/public/images/eso1540a/ (visited on 05/11/2023) (cit. on p. 2).

Fabry, M., P. Marchant, N. Langer and H. Sana (2023), *Modeling contact binaries*, **672** A175, URL: https://doi.org/10.1051%2F0004-6361%2F202346277 (cit. on pp. 2, 11, 38, 41).

Jermyn, A. S. et al. (2023), *Modules for Experiments in Stellar Astrophysics (MESA): Time-dependent Convection, Energy Conservation, Automatic Differentiation, and Infrastructure*, The Astrophysical Journal Supplement Series **265** 15, URL: https://dx.doi.org/10.3847/1538-4365/acae8d (cit. on pp. 1, 10).

Kippenhahn, R., A. Weigert and A. Weiss (2012), *Stellar Structure and Evolution*, eng, Second Edition, Astronomy and Astrophysics Library, Berlin, Heidelberg: Springer Berlin Heidelberg, ISBN: 9783642302558 (cit. on pp. 6, 10).

Langer, N., K. J. Fricke and D. Sugimoto (1983), *Semiconvective diffusion and energy transport*, **126** 207 (cit. on pp. 10, 13, 37).

Marchant, P. (2018), *The impact of tides and mass transfer on the evolution of metal-poor massive binary stars*, PhD thesis: Rheinische Friedrich-Wilhelms-Universität Bonn, URL: https://hdl.handle.net/20.500.11811/7507 (cit. on pp. 6, 8, 11–13, 16, 17, 37).

Marchant, P., N. Langer, P. Podsiadlowski, T. M. Tauris and T. J. Moriya (2016), *A new route towards merging massive black holes*, **588**, A50 A50, arXiv: 1601.03718 [astro-ph.SR] (cit. on pp. 1, 11, 38).

Menon, A. et al. (2021), *Detailed evolutionary models of massive contact binaries – I. Model grids and synthetic populations for the Magellanic Clouds*, Monthly Notices of the Royal Astronomical Society **507** 5013, URL: https://doi.org/10.1093%2Fmnras%2Fstab2276 (cit. on pp. 1–3, 10, 13–16, 18, 19, 22, 23, 29–31, 34, 36–38, 40–54).

MESA documentation (2023), URL: https://docs.mesastar.org/en/latest/reference/controls.html (visited on 07/10/2023) (cit. on p. 11).

Paxton, B. (2013), *MODULES FOR EXPERIMENTS IN STELLAR ASTROPHYSICS (MESA): PLANETS, OSCILLATIONS, ROTATION, AND MASSIVE STARS*, The Astrophysical Journal Supplement Series **208** 4, URL: https://dx.doi.org/10.1088/0067-0049/208/1/4 (cit. on pp. 10, 11).

Paxton, B., L. Bildsten et al. (2011), *MODULES FOR EXPERIMENTS IN STELLAR ASTROPHYSICS (MESA)*, The Astrophysical Journal Supplement Series **192** 3, URL: https://dx.doi.org/10.1088/0067-0049/192/1/3 (cit. on pp. 1, 10).

Paxton, B., P. Marchant et al. (2015), *MODULES FOR EXPERIMENTS IN STELLAR ASTROPHYSICS (MESA): BINARIES, PULSATIONS, AND EXPLOSIONS*, The Astrophysical Journal Supplement Series **220** 15, URL: https://dx.doi.org/10.1088/0067-0049/220/1/15 (cit. on p. 10).

Paxton, B., J. Schwab et al. (2018), *Modules for Experiments in Stellar Astrophysics (): Convective Boundaries, Element Diffusion, and Massive Star Explosions*, The Astrophysical Journal Supplement Series **234** 34, URL: https://dx.doi.org/10.3847/1538-4365/aaa5a8 (cit. on p. 10).

Paxton, B., R. Smolec et al. (2019), *Modules for Experiments in Stellar Astrophysics (MESA): Pulsating Variable Stars, Rotation, Convective Boundaries, and Energy Conservation*, The Astrophysical Journal Supplement Series **243** 10, URL: https://dx.doi.org/10.3847/1538-4365/ab2241 (cit. on p. 10).

Pols, O. (2009), *Stellar Structure and Evolution* (cit. on pp. 1, 4, 5, 9, 11, 37).

Postnov, K. A. and L. R. Yungelson (2014), *The Evolution of Compact Binary Star Systems*, Living Reviews in Relativity **17**, 3 3, arXiv: 1403.4754 [astro-ph.HE] (cit. on pp. 8, 9).

Schootemeijer, A., N. Langer, N. J. Grin and C. Wang (2019), *Constraining mixing in massive stars in the Small Magellanic Cloud*, **625**, A132 A132, arXiv: 1903.10423 [astro-ph.SR] (cit. on p. 13).

Schürmann, C., N. Langer, J. Kramer, P. Marchant and C. Wang (in prep.), *Analytic approximations for the outcome of mass transfer during core hydrogen burning in massive binary systems*, (cit. on p. 17).

List of Figures

List of Tables